Supplement of Atmos. Chem. Phys., 25, 12409–12431, 2025
https://doi.org/10.5194/acp-25-12409-2025-supplement

Supplement of

Formation and composition of organic aerosols from the uptake of glyoxal on natural mineral dust aerosols: a laboratory study

Francesco Battaglia et al.

Correspondence to: Paola Formenti (paola.formenti@lisa.ipsl.fr)

S1. New particle formation from water irradiation

S2. Protocols for the elemental and molecular analysis of the particle organic fraction

S3. Kinetic Analysis of Glyoxal Wall Loss under Varying Humidity Conditions

S4. Correction for dilution, wall loss and particle losses

S5. Control experiments of glyoxal with ammonium sulphate particles

S6. Content and composition of the organic fraction in the native Gobi dust aerosols

S7. Examples of results from SFE/GC-MS and ESI-Orbitrap of glyoxal-processed dust

Figure S1. Standard infrared absorption spectra of glyoxal, carbon monoxide, formic acid, and ozone (from bottom to top), with key absorption bands used for quantification marked by their central wavenumbers. All spectra are normalized to the maximum absorbance intensity of each compound to facilitate comparison. Shaded areas indicate spectral regions affected by water vapor absorption, which were excluded from the quantification of the target compounds. An example of spectrum recorded in the presence of water vapor at 80% relative humidity (RH) is shown (violet line).

Figure S2. Timeline of the ageing experiment D14, in which submicron dust was exposed to gas-phase glyoxal under humid conditions (78% RH) at 293 K and 1450 ppbv of ozone. (a) Time series of aerosol total number (grey) and volume (black) concentrations, derived from measured size distributions. (b) Mass concentrations of ammonium (yellow), sulfate (red), nitrate (blue), and organic compounds (green), as measured by the ACSM. The yellow-shaded area marks the period of irradiation, while green dashed vertical lines indicate the timing of glyoxal injection and red dashed vertical lines indicate the timing of ozone injection. All aerosol measurements have been corrected for dilution, wall losses, and losses in sampling lines.

Figure S3. Comparison of the time series of the logarithm of POM concentration (normalized to the initial value POM_0), upper panel, and the total volume concentration (normalized to the initial value Vol_0), lower panel. Time is calculated since the end of the dust injection. The slope of the linear decrease during the evaporation phase (straight solid lines) is indicated.

Figure S4. NO and NO_2 concentrations measured during the injection of water vapour in experiment D15. The shaded area corresponds to the injection of dust into the chamber, during which the instruments were disconnected. The yellow-highlighted portions indicate the interval where irradiation takes place. Wang et al. (2011) have shown that the chamber walls may act as a reservoir of a NO and HONO, that can be rapidly desorbed during the injection of water vapour. Upon irradiation, the desorbed HONO may act as a source of OH radicals, which in turn facilitate the rapid conversion of NO to NO_2.

Table S1. Instrumental and analytical setup for the analysis of the gas and aerosol phases presented in this study.

Table S2. List of target mass fragments for molecules linked to glyoxal reactivity used in the assignment of the SFE/GC-MS mass spectra. The table consists of three columns: the first column shows the masses of the fragments derived from molecules produced by the reactivity of glyoxal and mineral dust which are not present in the NIST library, the second column shows the expected molecular formulas of the fragments, and the third column describes the hypothesized molecular fragmentation pattern.

Table S3. List of filter samples collected for SFE-GC-MS and Orbitrap high-resolution mass spectrometry analyses, along with the corresponding experimental conditions. The experiments include dust only (D) and dust combined with glyoxal (D + GL). For selected experiments, filters were collected both in the dark or during irradiation (light). The RH values refer to the average relative humidity measured during the respective filter sampling periods. The presence of ozone (O_3) is indicated in the "Ox" column.

Table S4; List of experiments and their experimental conditions. $[Gly]_i$ is the initial concentration of glyoxal measured by the CAPS NO_2. The irradiation and relative humidity (RH) conditions are indicated.

Table S5. Result of J_{NO2} measurements for the experiments where irradiation tool place and the J_{gly} calculated from equation S3.7.

Table S6. Results of the kinetic study for glyoxal. The kinetic constants (expressed in s^{-1}) for the first-order processes are divided by type: glyoxal exchange equilibrium on dry walls ($k_{WL,Dry}$ and $k_{-WL,Dry}$), exchange equilibrium under humid conditions ($k_{WL,Humid}$ and $k_{-WL,Humid}$) and photolysis (k_{hydr} and J_{gly}). With the exception of J_{gly}, that is experimentally derived and constrained in the calculations, the constants are calculated by the kinetic model, while for the photolysis of glyoxal, the rate constants are calculated following the method described in paragraph S3.1.

Table S7. Control experiments using ammonium sulphate seed particles at 30% and 80% RH to validate the experimental protocols of glyoxal-dust interaction. Conditions include date, experiment ID, relative humidity (RH), light conditions, initial ozone ($[O_3]_i$) and glyoxal ($[Gly]_i$) concentrations in parts per billion volume (ppbv), temperature (Temp; K)), and initial volume concentration of seed particles ($Vseed_i$; μm^3 cm^{-3}). Initial concentrations ($[O_3]_i$, $[Gly]_i$ and $Vseed_i$) are referred to the maximum concentrations recorded after the injection.

Table S8. Particulate organic matter (POM) collected on filters and the number of ESI Orbitrap peaks detected under varying conditions of Gobi dust, including dry and humid (80% RH) environments, with exposure to light or dark.

S1. New particle formation from water irradiation

Water vapor used for ageing experiments is produced by heating water from an ultrapure water generation system (Milli-Q IQ 7000, Merk™), which contains a certain level of organic carbon contamination (2-3 µg L^{-1} according to the reading of the ultrapure water generation system). The gaseous organic carbon introduced with the water vapor might oxidize and form new particles, adding to the background organic aerosol concentration in the chamber, potentially forming additional particles that could interfere with the measurements of aerosol growth and transformation.

Dedicated experiments were conducted to assess this interference, as shown in **Figure S1. Figure S1** shows that the injection of water vapor is followed by a rapid and significant increase in the total number of particles, reaching a maximum value of about 27000 cm^{-3}, decreasing quickly, due to dilution but mostly coagulation, to a plateau value of approximately 5000 cm^{-3}.

The maximum total organic carbon concentration (TOC_{max}) that can be found in the chamber as a result of the water vapor injection can be estimated as

$$TOC_{max} = \left(\frac{w_{H_2O}}{w_{air}}\right) \times \left(\frac{\rho_{air}}{\rho_{H_2O}}\right) \times TOC_{H_2O} \qquad \text{(S1)}$$

where the ratio w_{H2O}/w_{air} is the percent mass fraction of water vapour introduced in CESAM at the maximum inner relative humidity and corresponding temperature (in this example 88%RH and 17°C, respectively), ρ_{air} and ρ_{H2O} are the corresponding air and the water densities (1.225 kg m^{-3} and 1 g cm^{-3}, respectively; (Jung and Schindler, 2019)), and TOC_{H2O} is the total organic carbon measured by the ultrapure water generation system (average of 2.2 µg L-^{1}). The calculation of the w_{H2O}/w_{air} ratio is done with the Humidity calculator application (https://humiditycalculator.vaisala.com/).

Upon reaching the plateau value of 5000 cm^{-3} in the particle number, lights are turned on and the particle concentration increases again up to approximately 20000 cm^{-3}, indicating that new particle formation due to photochemistry of the residual organic content in the gas phase is occurring. No particles are observed by the Scanning Mobility Particle Sizer (SMPS) (lower sizing limit of 19.5 nm). At this moment, the maximum mass particle concentration observed in the chamber can be calculated assuming a monodispersed particle distribution centered at an average diameter d_p of 10 nm as

$$N_{new} = \frac{4}{3}\pi \, {d_p}^3 \, \rho_p \;\; N_{CPC} \tag{S2}$$

Where N_{CPC} is the total number concentration measured by the Condensation Particle Counter (CPC) and ρ_p is the particle density, assumed equal to 1.2 g cm^{-3} (Kostenidou et al., 2007).

Finally, Figure S1 shows that the particle concentration starts decreasing after approximately 10 minutes, despite irradiation, suggesting that all the organic gas phase had undergone oxidation, and that coagulation and dilution are overtaking production. The mixing volume is further diluted to perform the dust injection (grey bar in Figure S1). By this procedure, the mass concentration finally measured by the SMPS in the size range smaller than 100 nm is 70 ng m^{-3}. For comparison, the dust mass concentration injected during this experiment is 102 µg m^{-3} (Table 1, assuming a density of 2.65 g cm^{-3}), for a minimum diameter of 150 nm.

Figure S2 summarizes the comparison of the calculations of TOC_{max} and N_{new}. The good agreement between the organic mass calculations supports the hypothesis that the aerosol originates from the oxidation of the TOC contained in the ultrapure water. The calculated mass concentration of organic particles is approximately one thousand times lower than the mass concentration of dust injected into the chamber, and the size distributions are not overlapping.

S2. Protocols for the elemental and molecular analysis of the particle organic fraction

S2.1. SFE/GC-MS

Supercritical fluid extraction coupled with gas chromatography mass spectrometry (SFE/GC-MS) is used to analyse the molecular composition of the aerosol organic fraction. It was originally developed by Chiappini et al. (2006) and was slightly modified by a Teledyne ISCO model 260D pump for the extraction step and a GC (Clarus 680 PerkinElmer) –MS (Clarus MS SQ8C Perkin Elmer) for the analysis.

The analytical protocol of the SFE/GC-MS analysis begins by placing the quartz filters inside an extraction cell. Prior to the extraction, 5 μL of two different solutions are deposited on the filters using a precision syringe (CR700-20 1-20ul (22s/2”/3), Hamilton, USA): (a) an internal standard solution composed by 20 μg mL^{-1} of Tridecane (99%, Sigma-Aldrich) and o-Toluic acid (Sigma Aldrich, purity >97 %) in dichloromethane (99.8 %, HPLC grade) and (b) a derivatizing agent solution composed by N,O-bis(trimethylsilyl)trifluoroacetamide (BSTFA) and 1% of trimethylchlorosilane as catalyst, provided by Sigma-Aldrich. The first step of the analysis is a static extraction, in which the cell is filled with supercritical CO_2 (LINDE, reference CO_2 High Purity), that interacts with the filter at 300 bar and 60°C, for 40 min. During this step, the trimethylsilylation of hydroxy and carboxy functions by BSTFA also occurs (generating trimethylsilyl (TMS) derivatives). The supercritical fluid containing the analytes is transferred to the GC injector through a deactivated silica transfer line. The injector is cooled at -20°C using liquid nitrogen flowing around the injector for 15 minutes, where the compounds are retained, and the gaseous CO_2 is removed. Once the extraction step was completed, the chemical analysis was continued with the injection of the condensed compounds by heat flash on the GC injector from -20°C to 280°C. The compounds are then eluted with helium flowing at 1 mL min^{-1} (Linde) and transferred to the GC (Clarus 680 PerkinElmer) for separation. The temperature gradient of the GC column (Rxi®-5Sil MS column (30 m, 0,25mmi.d., film thickness: 0.25 μm, Restek) goes from 60°C to 280°C at a rate of 5°C min^{-1} and held at 280°C for 10 min. Detection is achieved through electron impact (70 eV electron energy) ionisation followed by a quadrupole mass spectrometer (Clarus MS SQ8C Perkin Elmer) analysis that produces mass spectra from m/z 50 to m/z 300.

The data analysis is conducted using the proprietary software (TurboMass Version 6.1.0.1965 PerkinElmer®). The analysis is limited to the chromatographic peaks which elutes before the internal standards (around 42 minutes), as for higher retention times the signal to noise ratio is lower and not conclusive. The chromatograms of each filter sample are compared with those of the analytical and procedural blanks and a mass spectrum is extracted from each chromatographic peak that is not present in the blank. To account for the method variability in extraction efficiency concentrations are corrected using the internal standard o-Toluic acid TMS derivatives. The structural analysis of the molecule generating every chromatographic peak is then carried out using two methods. Each mass spectrum is compared with a reference spectra of the National Institute of Standards and Technology (NIST) Mass Spectral Library (Version 2.2), which assigns a structure to each spectrum with a relative probability (<80%). For spectra for which the automatic structural assignment fails (low assignment probability), we searched for target mass fragments derived from molecules linked to glyoxal reactivity (**Table S2**), in particular the 73 m/z fragment corresponding to a TMS derivatization $[Si(CH_3)_3]^+$, the 147 m/z fragment corresponding to two TMS derivatizations $[(CH_3)_2Si{=}OSi(CH_3)_3]^+$, the 131 m/z fragment (Glyoxylic acid TMS derivatized – CH_3), and 205 m/z fragment (Glyoxal monohydrate – CH_3).

Table S2. List of target mass fragments for molecules linked to glyoxal reactivity used in the assignment of the SFE/GC-MS mass spectra. The table consists of three columns: the first column shows the masses of the fragments derived from molecules produced by the reactivity of glyoxal and mineral dust which are not present in the NIST library, the second column shows the expected molecular formulas of the fragments, and the third column describes the hypothesized molecular fragmentation pattern.

m/z	Fragment	Assignment
73	$[Si(CH_3)_3]^+$	Fragment from compounds with 1 TMS functionality
117	$[COO{=}Si(CH_3)_3]^+$	Fragment from compounds with 1 TMS caboxylic functionality
131	$[(CH_3)_2SiO\text{-}C{=}O\text{-}HC{=}O]^+$	Glyoxylic acid fragment
147	$[(CH_3)_2Si{=}OSi(CH_3)_3]^+$	Fragment from compounds with 2 TMS functionalities
205	$[(CH_3)_3SiO\text{-}C{=}O\text{-}CH_2\text{-}OSi(CH_3)_2]^+$	Glycolic acid fragment
221	$[SiH(CH_3)_2\text{-}C_4H_4O_5\text{-}SiH_2]^+$	Glyoxal dimer fragment – 3*CH_3 + 3H

235	$[Si(CH_3)_3\text{-}C_4H_4O_5\text{-}SiH_2]^+$	Glyoxal dimer fragment – 2*CH_3 + 2H
263	$[Si(CH_3)_3\text{-}C_4H_4O_5\text{-}Si(CH_3)_2]^+$	Glyoxal dimer fragment from Gly hydrated ($C_2H_4O_3$) + Gly dihydrated ($C_2H_6O_4$) = $C_4H_6O_5$
281	$[Si(CH_3)_3\text{-}OSi(CH_3)_2\text{-}OSi(CH_3)_2\text{-}OSi(CH_3)H]^+$	Fragment from siloxane like compounds -> peak generated by GC column residues

S2.2. Electrospray ionization (ESI) high-resolution mass spectrometry

Molecular analysis of the organic fraction collected on the quartz filters is performed by electrospray ionization (ESI) high-resolution mass spectrometry (Kourtchev et al., 2015). A high-resolution (mass resolution=100000 at *m/z* 400) LTQ Orbitrap Velos mass spectrometer (Thermo Fisher, Bremen, Germany) equipped with a TriVersa Nanomate robotic nanoflow chip-based ESI source (Advion Biosciences, Ithaca NY, USA) is used to obtain high resolution mass spectra of the methanol extracts following an adaptation of the procedure described in Kourtchev et al. (2015). Filters are extracted one time in 1 mL of methanol (Optima TM grade, Fisher Scientific) and two times in 0.5 mL of methanol under ultrasonic agitation in slurry ice for 15 min. Extracts are combined and filtered sequentially through a 0.45 µm pore size and a 0.2 µm pore size Teflon filter (ISODiscTM Supelco), which are then reduced by volume to approximately 50–200 µL under a gentle stream of nitrogen. The resulting sample is injected by direct infusion. The negative ionization mass spectra are collected in three replicates at ranges m/z 50–500 and m/z 150–1000 and processed using Xcalibur 2.1 software (Thermo Scientific). In the settings of the data processing, the following atoms are included in the peak assignment: C (from 1 to 100 atoms in the possible assigned molecular formula), H (1-200), O (0-50), N (0-5), S (0-2), ^{13}C (0-1) and ^{34}S (0-1). The allowed mass accuracy in the formula assignment is ± 4 ppm.

The peak assignment to a molecular formula is done according to Zielinski et al. (2018). The protocol includes internal calibration, noise removal, blank subtraction, and additional atomic constraints for formula filtering: elemental ratios were set as $0.3 \leq H/C \leq 2.5$, $O/C \leq 2$, $N/C \leq 0.5$, $S/C \leq 0.2$, $^{13}C/^{12}C \leq 0.011$ and $^{34}S/^{32}S \leq 0.045$, and nitrogen rule. In the case of multiple assignments for the same peak, the formula with the lowest mass error was kept. This process allowed for the retrieval of parameters describing carbon oxidation, such as O/C and H/C ratios. Consequently, each mass spectrum was analysed to construct a Van Krevelen diagram, which is a graphical representation illustrating the sample composition in terms of carbon, oxygen, and hydrogen in the identified molecular formulas (Patriarca et al., 2018). Identified molecular formulas are categorised into the following groups: CHO, CHON, CHOS, CHNS, and CHONS.

A targeted search for molecular formulas resulting from glyoxal reactivity is also done. In this search, we included formulas associated with glyoxal chemical transformations such as hydration, oxidation, and oligomerization. Starting from the glyoxal formula, $C_2H_2O_2$, formulas for mono- and dihydration products are $C_2H_4O_3$ and $C_2H_6O_4$, respectively. Oxidation products included formic acid (CH_2O_2), glycolic acid ($C_2H_4O_3$), glyoxylic acid ($C_2H_2O_3$), and oxalic acid ($C_2H_2O_2$). Oligomers formed by the hydrolysis of hydrated glyoxal formulas were also sought. In the process of hydrolysis-driven oligomerization, each successive molecular addition results in the loss of a water molecule. If the oligomer is a ring, an additional water molecule is lost due to the condensation of the linear oligomer terminations. Denoting n as the number of molecules of the monohydrated form ($C_2H_4O_3$) and m as the number of molecules of the dihydrated glyoxal form ($C_2H_6O_4$) participating in the formation of an oligomer, the generated linear oligomers will have the formula $C_{2n+2m}H_{4n+6m-2(n+m-1)}O_{3n+4m-(n+m-1)}$, where the terms -2(n+m-1) and -(n+m-1) in the hydrogen and oxygen atom stoichiometry indicate water loss from the oligomerization process. For ring oligomers, formulas characterised by the stoichiometry $C_{2n+2m}H_{4n+6m-2(n+m)}O_{3n+4m-(n+m)}$ are searched. Similarly, formulas resulting from the condensation of hydrated forms with the listed organic acids are calculated and researched.

S2.3. X-ray photoelectron spectrometry (XPS)

X-ray photoelectron spectrometry (XPS) is used to quantify the elemental O/C ratio of the particle surface to a depth less than 10 nm. Measurements are performed with a VG ES-CALAB 250 instrument using monochromatic Al K_α radiation (1486.6 eV). The O/C ratio is quantified by integrating the areas of O_{1s} and C_{1s} peaks. This last is contributed by a number of functions, including $-CO_2$, C–O, C–C/C–H as well as C-F from the Teflon substrate. The contribution of the latter can be evaluated from the F1s (approximately 690 eV) as described in Denjean et al., (2015). The contribution of SiO_2 from the mineralogical composition of the dust to O1s was evaluated by integrating the Si2p peak

(107 eV) and applying the stoichiometric proportions between silicon and oxygen in the composition of quartz (O/Si = 2). The O/C_{surf} ratio is calculated as follows

$$O/C_{surf} = \frac{\mathbf{n[O_c]}}{\mathbf{n[C]}} = \frac{(\mathbf{n[O]-2n[Si]})}{\mathbf{n[C]}} \qquad \text{(S3)}$$

Where $\mathrm{n[O_c]}$ is the signal coming from oxygen bonded to carbon atoms only, $\mathrm{n[C]}$ is the signal of C_{1s}, $\mathrm{n[O]}$ the area from O_{1s} and n[Si] is the area of the signal from Si_{2p} that is multiplied by 2 to take into account the silica stoichiometry.

The XPS measurement on a filter collected during one ageing experiment are shown in Figure S3.

S3. Kinetic Analysis of Glyoxal Wall Loss under Varying Humidity Conditions

In this section, we present the experimental strategy adopted for the instrumental comparison in glyoxal detection and the calculation of the kinetic rates of its heterogeneous processes. Experiments considered are listed in **Table S4**.

Table S4. List of experiments and their experimental conditions. $[Gly]_i$ is the initial concentration of glyoxal measured by the CAPS NO_2. The irradiation and relative humidity (RH) conditions are indicated.

Exp	$[Gly]_i$	Exp. Objectives	Irradiation	RH%
1	0.9 ppm	1/ Instrumental inter-comparison and inter-calibration 2/ Wall loss kinetic in dry conditions	Dark	Dry
2	1.0 ppm	1/ Instrumental inter-comparison and inter-calibration 2/ Wall loss kinetic in dry conditions	Dark	Dry
3a	0.9 ppm	Wall loss kinetic in dry conditions	Dark	Dry
3b	0.7 ppm	1/ Gly wall loss kinetic at 30% RH 2/ Photolysis rate	Light	28 ± 1
4a	0.9 ppm	Wall loss kinetic in dry conditions	Dark	Dry
4b	0.8 ppm	1/ Wall loss kinetic at 50% RH 2/ Photolysis rate	Light	52 ± 2
5a	0.8 ppm	Wall loss kinetic in dry conditions	Dark	Dry
5b	0.7 ppm	1/ Wall loss kinetic at 80% RH	Dark	76 ± 2
6a	0.9 ppm	1/ Wall loss kinetic in dry conditions 2/ Photolysis rate	Light	Dry
6b	0.3 ppm	1/ Wall loss kinetic at 80% RH	Dark	81 ± 1

The first two experiments were conducted in dry conditions only. They consisted in consecutive injections of glyoxal until reaching around 1 ppm to compare the efficiency of detection of gas-phase glyoxal by Fourier Transform Infra-Red (FTIR), Proton Transfer Reaction-Time Of Flight-Mass Spectrometer (PTR-ToF-MS) and the Cavity Attenuated Phase Shift (CAPS) NO_2 instrument. After the last injection step, glyoxal was left in the chamber for the calculation of equilibrium kinetics on dry walls.

Figure S4 illustrates the timeline of Experiment n. 1 in dry conditions.

The second class of experiments (4 experiments) concerns the study of the partition and gas phase behaviour of the glyoxal in humid conditions, more relevant to the real atmosphere. This class includes four experiments, each one consisting of two phases. In the first phase (a), approximately 1 ppm of glyoxal was introduced into the dry chamber and left for several minutes for the calculation of dry partitioning kinetics. In the second phase (b), water vapour was injected into the chamber to study the partitioning kinetics of glyoxal on wet walls. In three experiments (3b, 4b and 6a), the chamber was irradiated to incorporate the photolysis of glyoxal into the system and enhance the realism of the conditions. The detection of glyoxal in humid conditions presents a number of challenges. Firstly, it is documented that the sensitivity of PTR-ToF-MS in glyoxal detection decreases with increasing RH (Stönner et al., 2017), compromising the accuracy of the instrumental comparisons at low glyoxal concentration. Secondly, as it will be discussed in detail in the following sections, glyoxal tends to rapidly adsorb onto the chamber walls, complicating both the injection of the target glyoxal concentration and the stabilization of the instrumental signal.

The results of the instrumental cross-comparisons in dry and humid conditions are presented in **Figure S5**.

With PTR-ToF-MS, the signal of protonated glyoxal ($CHOCHOH^+$) at 58.9312 *m/z* is systematically related with a fragment at a mass of 30.9829 *m/z*, which can be assigned to protonated formaldehyde (H_2COH^+), most likely originating from glyoxal fragmentation within the PTR drift tube (Stönner et al., 2017). This hypothesis is supported both by the high correlation between the two signals during the experiment (R^2=0.99; **Fig. S5a**) and the absence of formaldehyde in the chamber, confirmed by the analysis of the FTIR spectra (not shown).

The measurements by the FTIR and PTR-ToF-MS are perfectly correlated (R^2=0.98; **Fig. S5b**), both in dry and humid conditions. However, under humid conditions, the FTIR shows a better sensitivity than the PTR-ToF-MS, as expected. The intercomparison of the CAPS NO_2 with the PTR-ToF-MS and the FTIR (**Fig. S5c** and **Fig. S5d**, respectively) shows a very good agreement when the concentrations measured by the CAPS NO_2 are lower than approximately 600 ppbv. Above this value, the relation slightly deviates from linearity, and the CAPS NO_2 measurements are lower by about 15% with respect to both the PTR-ToF-MS and the FTIR.

An alternative explanation is that this effect could be attributed to the partial loss of glyoxal inside the PTFE tubing connecting the CAPS NO_2 to the simulation chamber. Losses of glyoxal in PTFE tubing have been previously observed and characterized (Min et al., 2016). On the contrary, the PTR-ToF-MS connection tubing is maintained at 60°C through a heating cover to prevent gas adsorption, and FTIR analysis is not affected by this phenomenon. Instrumental saturation is discarded as the glyoxal concentrations in the experiments are within the operating range of the instrument when converted to an equivalent NO_2 mixing ratio (measurement range 0 – 5000 ppb for glyoxal).

S3.1 Kinetic modelling

A modelling study was conducted to determine the kinetic rate constants of glyoxal in the chamber. The model adopted to describe the evolution of glyoxal concentration in the chamber consists in a system of differential equations, each one of those representing a process that leads to a variation in glyoxal concentration over time. The concentration of all the reactants is measured in units of molecules cm^{-3}. At time t_i the concentration of glyoxal in the gas phase is equal to:

$$[Gly]_{g,t_i} = [Gly]_{g,t_{i-1}} + d[Gly]_g \tag{S4}$$

The term $d[Gly]_g$ represents represents the variation of glyoxal due to the sum of all the processes affecting its concentration in the simulation chamber occurring from t_{i-1} to t_i with a rate defined as $\frac{d[Gly]_g}{dt}$, that is expressed as follows:

$$\frac{d[Gly]_g}{dt} = -\frac{d[Gly]_{g,dil}}{dt} - \frac{d[Gly]_{g,photo}}{dt} - \frac{d[Gly]_{g,WL}}{dt} + \frac{d[Gly]_{W,-WL}}{dt} \tag{S5}$$

The first term ($\frac{d[Gly]_{g,dil}}{dt}$) represents the loss of glyoxal due to the dilution of the reagents mixture in the chamber due to the compensation of the instrumental sampling flow in order to keep a constant pressure in the chamber.

The dilution process follows a first-order kinetic, expressed from the following reaction:

$$Gly_g \xrightarrow{k_{dil}} \emptyset \tag{S6}$$

and expressed by the following kinetic law:

$$\frac{d[Gly]_{g,dil}}{dt} = -k_{dil}[Gly]_{g,t} \tag{S7}$$

where $k_{dil}(s^{-1})$ is the time – dependent first – order dilution rate constant, which can be experimentally derived from the following expression:

$$k_{dil} = \frac{\Phi}{V} \tag{S8}$$

Where Φ (L s^{-1}) represents the compensation flow inside CESAM, and V is the volume of the chamber, equal to 4.2 m^3. The dilution rate depends from the number and the sampling rates of the instruments used, but usually falls in the range of approximately $10^{-7} – 10^{-4}$ s^{-1}.

The second term of equation (S3.2) ($\frac{d[Gly]_{g,photo}}{dt}$) describes the first-order photolysis rate of glyoxal, denoted as j_{gly}, through which, in the presence of light, glyoxal can undergo photo dissociation leading to the formation of various products:

$$Gly_g + h\nu \xrightarrow{J_{gly}} products \quad \text{(S9)}$$

This process is described by the following kinetic law:

$$\frac{d[Gly]_{g,photo}}{dt} = -j_{gly}[Gly]_{g,t} \quad \text{(S10)}$$

The first order photolysis frequency of glyoxal (J_{gly}) was estimated from known cross section and quantum yields of glyoxal (Tadić et al. 2006, Atkinson et al. 2006, respectively) and the CESAM photolytic light flux (expressed as J_{NO2}), which is regularly checked through the NO_2 photolysis actinometric method (Doussin et al., 2023). The general expression of the photolysis first order rate constant is for the molecule x at a fixed temperature, J_x is equal to:

$$J_X = \int \sigma_x(\lambda)\varphi_x(\lambda)\, I(\lambda)d\lambda \quad \text{(S11)}$$

Where $\sigma_x(\lambda)$ is the molecular cross section, $\varphi_x(\lambda)$ is the quantum yield and $I(\lambda)$ is the irradiance of the light source. By directly measuring J_{NO2} in CESAM as described in Wang et al. (2011), it is possible to retrieve the theoretical value of J_{gly} at the same wavelengths by applying:

$$J_{gly} = J_{NO_2}\frac{\int \sigma_{gly}(\lambda)\varphi_{gly}(\lambda)d\lambda}{\int \sigma_{NO_2}(\lambda)\varphi_{NO_2}(\lambda)d\lambda} \quad \text{(S12)}$$

We calculated J_{gly} in the range between 300 and 500 nm, applying literature data at 298K: $\varphi_{gly}(\lambda)$ from (Tadić et al., 2006), $\varphi_{NO_2}(\lambda)$ from (Gardner et al., 1987), $\sigma_{NO_2}(\lambda)$ and $\sigma_{gly}(\lambda)$ by Atkinson et al. (2004) and Atkinson et al. (2006), respectively (**Table S5**).

Table S5. Result of J_{NO2} measurements for the experiments where irradiation tool place and the J_{gly} calculated from equation S3.7.

Exp.	RH (%)	T (K)	Light	J_{NO2} (s^{-1})	J_{gly} (s^{-1})
3	30%	294.15	Light	6.3E-03	1.7E-04
4	50%	295.65	Light	6.3E-03	1.7E-04
6	80%	290.95	Light	7.5E-03	2.0E-04

The third and fourth terms of equation S3.2 ($\frac{d[Gly]_{g,WL}}{dt}$ and $\frac{d[Gly]_{W,-WL}}{dt}$) refer to the process of reversible exchange of glyoxal on the chamber walls. In accordance with what is generally considered for wall losses (Grosjean et al., 1985, Doussin et al., 2023), it is based on the assumption that the effects of the chamber walls on glyoxal are equilibria described by an adsorption and a desorption terms, both of first order, as shown in reaction S3.3:

$$Gly_g \underset{k_{-WL,Gly}}{\overset{k_{WL,Gly}}{\rightleftharpoons}} Gly_W \tag{S13}$$

The kinetic law describing this equilibrium process, that is integrated in the model, is the following:

$$-\frac{d[Gly]_{g,WL}}{dt} + \frac{d[Gly]_{W,-WL}}{dt} = -\,k_{WL}[Gly]_{g,t} + k_{-WL}[Gly]_{W,t} \tag{S14}$$

Where k_{WL} and k_{-WL} indicate the rate constants for adsorption and desorption. The equilibrium constants for the wall loss process ($K_{eq,gly}$) is derived from the ratio of the forward to the reverse rate constants. $[Gly]_{W,t}$ is the reservoir concentration of glyoxal on the walls, described by:

$$[Gly]_{W,t} = [Gly]_{g,0} - [Gly]_{g,t} - \int_0^t (k_{dil}[Gly]_{g,t} + j_{gly}[Gly]_{g,t})dt \qquad \text{(S15)}$$

Where $[Gly]_{g,0}$ is the initial concentration post glyoxal injection (i.e. after injection glyoxal maximum concentration), $[Gly]_{g,t}$ is the concentration in the chamber at time t, and the integral represents the total amount of compound that has been removed from the chamber by processes other than wall loss, up to time t.

For each experiment, starting from the point of maximum glyoxal concentration after injection, we applied the kinetic equations presented in this paragraph. Using equations (S3.1) and (S3.2), we recalculated the time evolution of glyoxal concentration, accounting for the processes of wall loss, photolysis, and dilution. This approach allowed us to model the concentration decay and compare it with experimental data under various humidity conditions.

The rate constants for wall losses were calculated by minimising the residual sum of squares between the experimentally measured glyoxal concentrations and those provided by the model by applying a nonlinear optimization using the generalized reduced gradient (GRG) algorithm (Lasdon et al., 1974) using the Microsoft Excel 2016 Solver.

S3.2 Results

Figure S6 shows the timelines of the CAPS NO_2, FTIR and PTR-ToF–MS measurements for Experiment 5 conducted at RH reaching 80%. After the water vapour injection, the glyoxal concentrations measured by the CAPS NO_2 and the PTR-ToF-MS rapidly decrease and disappear in approximately 5 minutes when the RH exceeds 60%. The rapid glyoxal concentration decline suggests that in humid conditions, the CAPS NO_2 system may experience a loss of glyoxal in the tubing, possibly due to condensation or interactions with water vapour. Additionally, the PTR-ToF-MS is interested by reduced sensitivity to glyoxal at higher RH, which could affect its accuracy in measuring glyoxal concentrations in such environments. In contrast, the glyoxal concentration measured by FTIR decreases at a slower rate than CAPS NO_2, indicating that FTIR is less affected by humidity.

For these reasons, we preferred to use FTIR as the reference technique for monitoring glyoxal concentration under humid conditions, as it provides more reliable measurements compared to CAPS NO_2 and PTR-ToF-MS, which are susceptible to losses in glyoxal detection in the presence of water vapour.

To ensure accuracy, we verified the stability of the FTIR glyoxal signal under humid conditions. This step was necessary to confirm that the FTIR measurements were not significantly influenced by water vapour, ensuring reliable monitoring of glyoxal concentrations even at higher RH levels. To do this, we checked that no other signals appeared in the integration range and that there was no modification in the shape of the glyoxal absorption band (**Figure S7**). Additionally, we performed a manual integration of the band, confirming that the intensity results from the manual integration were superimposable with the concentrations calculated by the deconvolution method.

The calculations of the kinetic constants were performed separately for each experiment, to account for the fact that the heterogeneous kinetics of glyoxal may depend on the state of the chamber walls, unique to each experiment and challenging to replicate.

Figure S8 shows that the constants calculated and implemented in the simplified kinetic model accurately describe the experimental data (experiment 6).

Table S6 summarises the rate constants calculated for each experiment.

Table S6. Results of the kinetic study for glyoxal. The kinetic constants (expressed in s^{-1}) for the first-order processes are divided by type: glyoxal exchange equilibrium on dry walls ($k_{WL,Dry}$ and $k_{-WL,Dry}$), exchange equilibrium under humid conditions ($k_{WL,Humid}$ and $k_{-WL,Humid}$) and photolysis (k_{hydr} and J_{gly}). With the exception of J_{gly}, that is experimentally derived and constrained in the calculations, the constants are calculated by the kinetic model, while for the photolysis of glyoxal, the rate constants are calculated following the method described in paragraph S3.1.

			Wall loss dry			**Wall loss humid**			**Photolysis**
Exp.	RH (%)	T (K)	$k_{WL,Dry}$ (s^{-1})	$k_{-WL,Dry}$ (s^{-1})	$K_{eq,dry}$	$k_{WL,Humid}$ (s^{-1})	$k_{-WL,Humid}$ (s^{-1})	$K_{eq,humid}$	J_{gly} (s^{-1})
1	Dry	294.15	1.97E-05	3.57E-05	5.52E-01	---	---	---	---
2	Dry	295.65	4.46E-05	3.37E-05	1.32E+00	---	---	---	---
3	Dry; 30%	296.15	4.46E-05	3.37E-05	1.32E+00	8.00E-04	6.00E-05	1.33E+01	$1.7 \cdot 10^{-4}$
4	Dry; 50%	290.95	9.60E-05	3.57E-05	2.69E+00	6.76E-04	4.80E-05	1.41E+01	$1.7 \cdot 10^{-4}$
5	Dry; 80%	294.15	1.24E-04	3.55E-05	3.49E+00	1.82E-03	7.38E-05	2.47E+01	---
6	Dry; 80%	295.65	1.05E-04	3.55E-05	2.96E+00	2.20E-03	7.00E-05	3.14E+01	$2.0 \cdot 10^{-4}$

The removal of glyoxal by the chamber walls results to be reversible under both dry and humid conditions. For equivalent experiments, the wall partitioning rate constants related are reasonably similar, within the variability induced by the conditions of the chamber walls. The wall loss constants under humid conditions, and their reverse processes, are larger (up to approximately two orders of magnitude) than their dry counterparts.

The average glyoxal's wall loss kinetic constant is 8 (± 4) × 10^{-5} s^{-1} in dry conditions ($k_{WL,Dry}$) and 1.3 (± 0.9) × 10^{-3} s^{-1} in humid conditions ($k_{WL,Humid}$). This behaviour was already observed in experiments in the Caltech Teflon chamber (Loza et al., 2010), for which the first order wall loss rate constant at 61% RH was about 50 times higher than in dry conditions ($k_{WL,Humid} = 4.7 \times 10^{-5}$ s^{-1} and $k_{WL,Dry} = 9.6 \times 10^{-7}$ s^{-1}). However, the rate constants reported by Loza et al. (2010) are two order of magnitude lower than our evaluation. This fact cannot be explained by the different surface-to-volume ratio of the two chambers, as the one of CESAM is only 4 times larger than the one of the Caltech chamber. A possible explanation could be the fact that the Teflon is highly hydrophobic. The partitioning of glyoxal on the walls appears to be reversible.

S4. Correction for dilution, wall loss and particle losses

S4.1 Dilution correction

The dilution of the gas-phase compounds and aerosol particles in the chamber during the experiments is due to the injection of particle-free nitrogen flow, which is needed to equalise the flow extracted by the instruments and keep the pressure constant in the chamber. The differential decrease in concentration due to dilution ($\Delta C_{dilution_{t_n}}$) in a generic time interval from t_{n-1} to t_n is calculated according to the procedure described in Denjean et al. (2015) as:

$$\Delta C_{dilution_{t_n}} = C_{t_{n-1}} \cdot \left(-\frac{Q_{t_{n-1}}}{V_{chamber}}\right) \cdot e^{-\left(\frac{Q_{t_{n-1}}}{V_{chamber}}\right)\cdot(t_n - t_{n-1})} \cdot (t_n - t_{n-1}) \qquad \text{(S16)}$$

where $C_{t_{n-1}}$ is the concentration measured at time t_{n-1}, $\frac{Q}{V_{chamber}}$ is the dilution rate constant in the chamber (s^{-1}), with Q being the compensation air flow ($L\ s^{-1}$) and $V_{chamber}$ the inner volume of CESAM (4200 L).

S4.2 Particle losses

Beside dilution, aerosol particles undergo size-dependent losses due to interactions with the chamber walls (wall losses) and the connecting tubes to the instruments (particle losses). The corrected particle concentration within the chamber can be estimated as

$$C(D)_{corrected_{t_n}} = \left(C(D)_{measured_{t_n}} - C(D)_{measured_{t_{n-1}}}\right) - \Delta C(D)_{dilution\&wall\ loss_{t_n}} \qquad \text{(S17)}$$

S4.2.1 Wall losses

The size-dependent particle wall losses are caused by the collisions of the particles with the chamber walls. The differential increase in concentration due to wall loss ($\Delta C_{wall\ loss_{t_n}}$) in a generic time interval t_{n-1} to t_n can be calculated as:

$$\Delta C(D)_{wall\ loss_{t_n}} = W_{t_{n-1}}(D) \cdot \left(-wlr(D)\right) \cdot e^{-wlr(D)\cdot(t_n - t_{n-1})} \cdot (t_n - t_{n-1}) \qquad \text{(S18)}$$

where *wlr*(*D*) indicates the size-dependent wall loss rate constant (s^{-1}). **Figure S9** shows *wlr*(*D*) calculated for mineral dust particles (mass density 2.65 g m^{-3}) adapting the model of Lai and Nazaroff (2000) to the CESAM chamber, as discussed in Lamkaddam (2017).

For instruments that provide size-integrated concentrations (e.g., ACSM), the wall loss correction was calculated as the ratio between the calculated size-integrated concentration estimated on their working range from SMPS/Sky-GRIMM Optical Particle Counter (OPC) measurements, and the measured concentration as

$$\%(wall\ loss)_{t_n} = \frac{C_{corrected\ wall\ loss_{t_n}}}{C_{measured_{t_n}}} \qquad \text{(S19)}$$

S4.2.2 Aspiration and transmission losses

The size-dependent losses ($L(D_i)$) of aerosol particles between the chamber and the instruments are due to losses in the connection tubes when the particles are aspirated from the chamber (sampling losses) and while the particles within the tubes (transmission losses). These can be corrected using the Particle Loss Calculator (PLC; Von der Weiden et al., 2009) using as input the geometry of the sampling line, the sampling flow rate, the particle shape factor, and the particle density. The particle loss functions for the sampling lines of the SMPS, Sky-GRIMM, CPC and Time-of-flight Aerosol Chemical Speciation Monitor (ToF-ACSM) are illustrated in **Figure S10**. On the size range of interest of this work (0.1 – 1 µm), the particle losses are minor (within 6%) and most important almost equal from one instrument to the other, which makes the various measurements comparable. For these reasons, particle loss corrections were not applied to the measured particle concentrations.

S5. Control experiments of glyoxal with ammonium sulphate particles

Five control experiments using ammonium sulphate as seeds were conducted at 30 and 80% RH to validate the experimental protocol. **Table S7** summarizes the control experiments and the associated conditions.

Table S7. Control experiments using ammonium sulphate seed particles at 30% and 80% RH to validate the experimental protocols of glyoxal-dust interaction. Conditions include date, experiment ID, relative humidity (RH), light conditions, initial ozone ($[O_3]_i$) and glyoxal ($[Gly]_i$) concentrations in parts per billion volume (ppbv), temperature (Temp; K)), and initial volume concentration of seed particles ($Vseed_i$; $\mu m^3\ cm^{-3}$). Initial concentrations ($[O_3]_i$, $[Gly]_i$ and $Vseed_i$) are referred to the maximum concentrations recorded after the injection.

Conditions	**Date**	**ID**	**RH**	**Light**	**$[O_3]_i$ ppb_v**	**Temp, K**	**$[Gly]_i$ ppb_v**	**$Vseed_i$ $\mu m^3\ cm^{-3}$**
AS+GL	21/02/2023	AS_1	38%	dark	---	298	527	50.1
AS+GL	23/02/2023a	AS_2	35%	dark	---	298	516	48.3
AS+GL	23/02/2023b	AS_3	32%	light	---	298	445	64.8
AS+GL	07/02/2023	AS_4	81%	light	---	301	2000	304.1
AS+GL	08/02/2023	AS_5	83%	light	---	300	1000	161.2

Ammonium sulphate particles were generated by vaporizing a solution of 0.1 M high-purity ammonium sulphate (Sigma-Aldrich, 99.99%) using a constant-output atomizer (model 3076, TSI Inc., Shoreview, MN, USA) with at a nitrogen flow of 2 L min^{-1}. Prior entering the chamber, the solution was dried using a diffusion dryer (model 3062, TSI Inc., Shoreview, MN, USA) and size-selected using the AAC (D_m = 400 nm, k = 1770 kg m^{-3}, f = 3) with a sheath flow of 8 L min^{-1}. Unlike the dust injection protocol, it was not necessary to modify the internal chamber pressure to achieve a sufficient inflow of ammonium sulphate particles.

The timeline of the experiments is shown in **Figure S11**, presenting a time series of normalized intensities for various organic fragments detected by the ACSM, specifically m/z 58, 68, 105, 44, and total organic fraction, normalized against the sulphate signal. These specific signals are chosen because they serve as key markers for different aspects of glyoxal chemistry: m/z 58 is a marker for glyoxal itself, m/z 105 indicates glyoxal oligomers, m/z 68 represents imidazole-like CHON structures formed through the glyoxal-ammonium sulphate reaction, and m/z 44 is commonly associated with secondary organic aerosol (SOA) formation.

This graphical representation mirrors the dilution experiments described by Galloway et al. (2009) to track the dynamics and transformations of glyoxal and its reaction products in the aerosol phase. Galloway et al. (2009) examined the behaviour of glyoxal (GL) uptake and SOA formation by monitoring the time traces of total organics and specific fragment ions (m/z 58, 105, and 68) normalized by the sulphate ion signal. Their experimental protocol consisted in injecting glyoxal continuous until reaching the equilibrium with the walls, when the seed aerosols are injected. As a consequence, the formation of SOA occurs on a longer time scale, and reaches a maximum after approximately 10 hours. **Figure S12** presents the time traces of glyoxal concentration, total organics, and specific fragment ions from two experiments in dark and irradiated conditions. At the point of glyoxal dilution, indicated by a black vertical line, the normalized signals for total organics and GL marker ions (m/z 58 and 105) decreased by 30% and 17%, respectively, suggesting that the uptake of glyoxal is reversible.

Figure S12 shows that the behaviour of the m/z 68 marker, associated with imidazole, is different as its uptake is irreversible. This is also true for m/z 44 under irradiation conditions, suggesting that the organic fraction of the aerosol continues to be oxidised with time. This is observed in our experiments too, at 80% RH, when irradiation promote the m/z 44 signal with respect to the dark conditions. This effect is observed at 30%, but less pronounced. This suggests that irradiation od the AS/glyoxal system increases upon irradiation.

Similar to what observed in Galloway et al. (2009), in our experiments, after the peak of glyoxal uptake, the normalized organic concentration and tracer signals of glyoxal and its oligomers (m/z 58 and 105) decreases over time, suggesting that the uptake is reversible. The behaviour of imidazole is different from that observed by Galloway, as in our experiment this compound shows a reversible uptake, albeit at a slower rate than fragments m/z 58 and 105. We attribute this difference to the fact that, in our study, we performed a single injection of glyoxal, which is then rapidly lost from exchanges with the walls, particularly at 80%RH.

In addition to m/z= 44, 58, 68 and 105, Galloway et al. (2009) observed significant fragments at m/z 29, 77, 88, 117, 135, 145, and 175. These fragments are associated with precursor structures originating from glyoxal, along with its hydration and oligomerization products, which aligns with the findings from Liggio et al. (2005).

Figure S13 illustrates the ACSM organic fraction mass spectra recorded at maximum glyoxal uptake on ammonium sulphate experiments. Beside the major fragments m/z 29, 58, 30 and 44, the m/z 79 fragment is observed during 3 out of 5 experiments and attributed to organosulphates by Galloway et al. (2009). No significant differences are observed at different RH nor according to irradiation.

S6. Content and composition of the organic fraction in the native Gobi dust aerosols

Control experiments on monodisperse submicron dust aerosol particles without chemical interaction were conducted in dry conditions, at 50% and at 80 RH% to evaluate the quantity and the composition of native organic fraction.

The average ratio of the organic mass with respect to the total dust mass (F_{org}) is 5.1 ± 0.4 for RH < 12%, and 5.4 ± 0.8 for RH at 80%.

Figure S14 compares the mass spectra measured by the ACSM in dry and humid conditions (50% and 80%), with and without irradiation.

The most intense peaks consistently appear at m/z = 18, 28, and 44, across all conditions. The peak at m/z = 18 corresponds to water (H_2O), a known fragment in mass spectrometry that can increase under higher RH conditions. Peaks at m/z = 28 and m/z = 44 represent oxygenated organic compounds. Overall the organic composition of Gobi dust appears to be remarkably consistent in terms of oxidation state. Whether the dust is subjected to different levels of RHor to light exposure, no noticeable changes in the organic fraction is observed in dry conditions. In addition, the stability of the m/z 18 fragment across different RH conditions suggests that Gobi dust particles maintain limited but measurable hygroscopicity. The comparison also shows that the chamber conditions do not affect the organic composition of the dust, as the measurements compare very well with those performed with the simplified setup.

S6.3. ESI Orbitrap

Table S8 presents the quantity of particulate organic matter (POM) estimated by integrating the mass concentration measured by the ACMS over the time period of the filter collection, alongside the number of signals detected through ESI Orbitrap analysis.

Table S86. Particulate organic matter (POM) collected on filters and the number of ESI Orbitrap peaks detected under varying conditions of Gobi dust, including dry and humid (80% RH) environments, with exposure to light or dark.

Conditions	POM (µg)	Number of ESI Orbitrap peaks detected
Gobi dust, dry, dark	0.4	270
Gobi dust, dry, light	0.3	145

Gobi dust, 80% RH, dark	0.9	102
Gobi dust, 80% RH, light	0.8	86

The POM concentration is low regardless of the collected on the filters varies across different conditions, with the highest POM observed under dark, humid conditions (0.9 µg) and the lowest under dry, light conditions (0.3 µg). The POM values are at the lower limit of the working range for ESI-MS analysis, which could affect the sensitivity and reliability of peak detection.

The mass spectra collected in dry conditions and at 80%RH, with and without irradiation are shown in **Figure S15.** The analysis does not detect any glyoxal-related organic compounds, which is the necessary baseline for interpreting the results of the uptake experiments.

The molecular composition of the native dust from the ESI Orbitrap measurements show a low number of peaks and a possible signal suppression to matrix effects. The mass spectra under dry conditions reveal a complex mixture of compounds, particularly with prominent peaks in the lower m/z range (< 500 m/z), with a predominance of CHON and CHONS compounds, while CHO compounds are less represented. When exposed to light under dry conditions, there is a noticeable decrease in peak intensity and a shift of CHOS signals towards higher oxidation states in the Van Krevelen diagram suggesting possible oxidation and photolysis of the native organic matter. The fact that the ACSM showed an invariant oxidation state suggests that the changes may involve a minor fraction of the native organic matter with higher ionisation potential in ESI Orbitrap. Under humid conditions, no appreciable changes in oxidation state or peak number are observed.

The bulk composition analysed by ESI Orbitrap probably consists predominantly of lipidic and proteinaceous compounds, as indicated by the presence of signals from molecules containing C, H, O, N, and S. In particular, the O/C ratio measured with the highest frequency remains in fact relatively stable across the four conditions (dark and irradiated, in both dry and 80% RH environments). In dry conditions, the dark samples show a peak O/C ratio around 0.2, indicating that the most common compounds have a relatively low level of oxidation. When these samples are irradiated, the O/C ratio with the highest frequency shifts slightly higher, peaking around 0.3 to 0.4. At 80% RH condition, the dark samples maintain a similar O/C ratio peak near 0.2, comparable to the dry dark samples. Under irradiation at 80% RH, the O/C ratio at maximum frequency remains stable, with values between 0.1 and 0.2, showing consistency across the different conditions.

S6.4. SFE-GC-MS

Figure S17 shows the chromatograms from the SFE-GC-MS analysis of Gobi dust's organic fraction. The chromatograms display a retention time interval between 34 and 38 minutes. This specific interval is chosen because no significant peaks are detected before 34 minutes, while after 38 minutes, the chromatograms are dominated by the signals from the two added internal standards. Besides, they become too noisy, making it difficult to extract reliable chemical information.

In the temporal window under analysis, the chromatograms exhibit poor reproducibility across different experimental conditions. Some compounds are identified. Lactic acid is found in three out of the four chromatograms, but not in dry and dark conditions. Other compounds, such as 3,3,5-trimethylcyclohexanone, n-octanol, and benzyl alcohol, were only detected in the sample processed under irradiation at 80% RH. We exclude the possibility that these compounds originate from a photochemical transformation of the organic material in the dust, as the corresponding chromatogram of the sample collected in dark conditions does not show the precursor products that we observe under irradiation. This suggests that compounds are part of the dust's organic content but are not consistently detected across all conditions. Several peaks marked with asterisks remain unassigned, as the corresponding mass spectra did not match reference spectra in the NIST library with sufficient probability (≥80%).

Despite the observed variability, the key finding is that none of the detected compounds are related to glyoxal. In summary, the results indicate that the organic composition of dust aerosols is shaped less by experimental conditions (humidity, light) and more by the inherent variability of the dust itself. Levulinic acid and lactic acid, could share a biological origin with the CN and CNO signals already observed in dust particle mass spectra. Both results suggest that biological material or its degradation products are mixed with the dust aerosol, contributing to the complexity of the organic fraction (Carr et al., 2002; Kim et al., 2024). In prior investigations concerning organic acids in dust samples, a variety of linear

(C1-C10), branched chain, and hydroxy (lactic and glycolic) monoacids in dust samples was observed. Notably, lactic acid was abundant in aerosol samples collected from North East China, attributed to microbial and plant sources (Mochizuki et al., 2018). Kawamura et al. (2000) analysed urban dust and soil samples from the atmosphere of Los Angeles and detected carboxylic acids in the dust organic fraction. Organic acids were not detected in the soils, but only in the dust samples at concentrations ranging from 200-770 nmol g^{-1}. Benzoic acid was detected in dust samples, while we detect its reduced form (benzylic alcohol). Furthermore, GC analysis from Gobi dust samples (< 10 µm) from Mt. Tateyama (Japan) indicates the presence of lactic and glycolic acids (Mochizuki et al., 2016). The authors suggest that these organic acids are adsorbed onto dust particles during transport, making dust particles carriers of volatile and semi-volatile organic acids.

S7. Examples of results from SFE/GC-MS and ESI-Orbitrap of glyoxal-processed dust

Figure 18 shows the gas chromatograms obtained for experiments D_2, D_{13}, D_{15} and D_{16} at 80% RH, with and without irradiation, with and without ozone (**Table 1** in the main text).

The chromatograms of samples collected in the presence of glyoxal generally exhibit a higher number of peaks compared to samples of dust-only, indicating glyoxal oxidation and production of organic aerosols. A higher number of peaks are detected in samples after irradiation compared to dark conditions. This suggests that the exposure to light influences the chemical composition of the samples by promoting pathways that alter the chromatogram profile, possibly through photochemical reactions, which could lead to glyoxal oxidation products. However, in the presence of ozone and glyoxal, the chromatogram profile recorded under dark conditions is comparable to that recorded in the presence of light, suggesting that ozone may also play a significant role in the glyoxal oxidation process, driving similar chemical reactions in both light and dark environments. This could imply that the oxidative capacity of ozone is sufficient to promote glyoxal oxidation and organic formation independently of photolytic processes, resulting in comparable chromatogram profiles regardless of the presence of light. Lactic and levulinic acids are detected in 10 and 9 samples, respectively, regardless of the experimental conditions. Compounds detected less frequently include benzyl alcohol, 3,3,5-trimethylcyclohexanone, methylphosphonic acid (5 samples), decanal (4 samples), and various organic acids, including heptanoic, propanedioic, and hydroacrylic acids (3 samples), as well as benzoic acid and 1-octanol (2 samples).

An example of mass spectrum from ESI-Orbitrap analysis and assigned formula is shown in Figure 19.

Figure S1. Total particle number concentration (black line) measured by the Condensation Particle Counter (CPC) instrument following the injection water vapour, indicated by a vertical blue bar, for one experiment conducted at 80% Relative Humidity (RH) (blue line). The irradiation is indicated by the vertical yellow bars. The vertical orange bar indicates the time of injection of mineral dust particles. The vertical green bar indicates the time of injection of glyoxal. The grey area indicates the time interval where the instruments were disconnected for dust injection. The Total Organic Carbon (TOC) of the ultrapure water injected for this experiment was 2.2 µg L^{-1}.

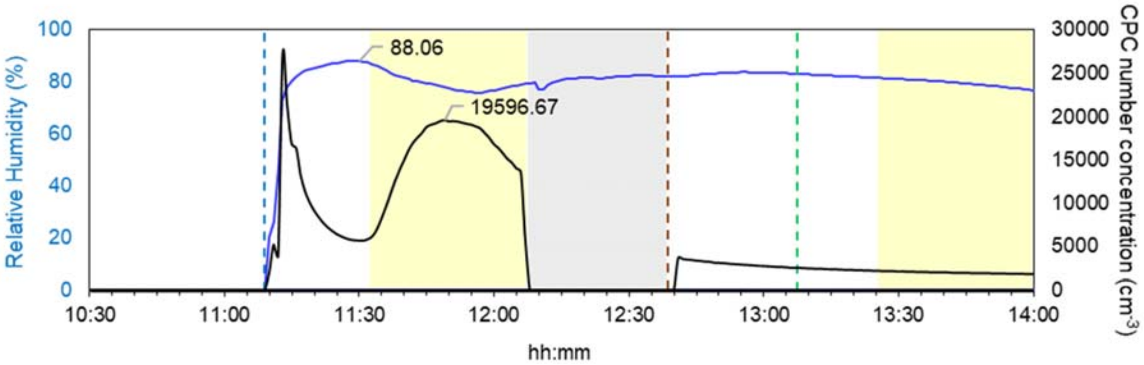

Figure S2. Mass concentration calculations following the injection of water vapour and irradiation for 11 experiments with glyoxal only (experiment type GL), dust only and dust aged with glyoxal (D). The blue bars represent the organic masses calculated based on the relative humidity (RH) in the chamber from TOC_{max} calculated by Eq. S1.1, while the green bars indicate the masses calculated from the measured particle concentration measured by the CPC as SOA_{NPF} from Eq. S1.2.

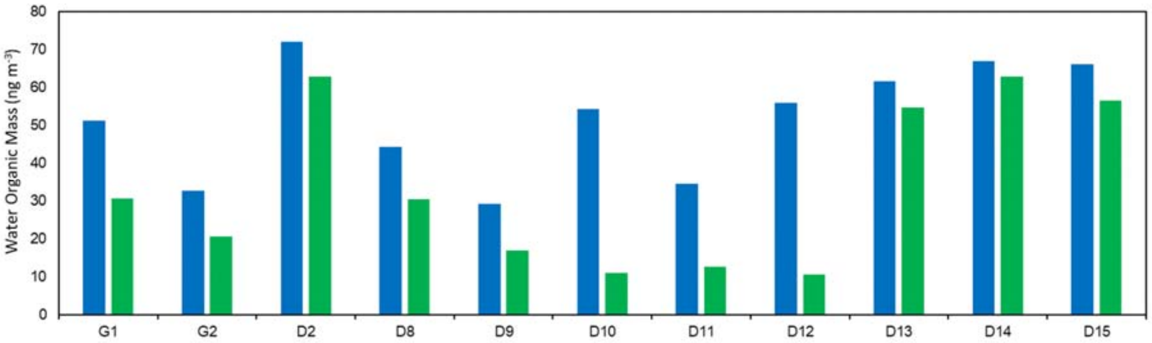

Figure S3. Standard infrared absorption spectra of glyoxal, carbon monoxide, formic acid, and ozone (from bottom to top), with key absorption bands used for quantification marked by their central wavenumbers. All spectra are normalized to the maximum absorbance intensity of each compound to facilitate comparison. Shaded areas indicate spectral regions affected by water vapor absorption, which were excluded from the quantification of the target compounds. An example of spectrum recorded in the presence of water vapor at 80% relative humidity (RH) is shown (violet line**)**.

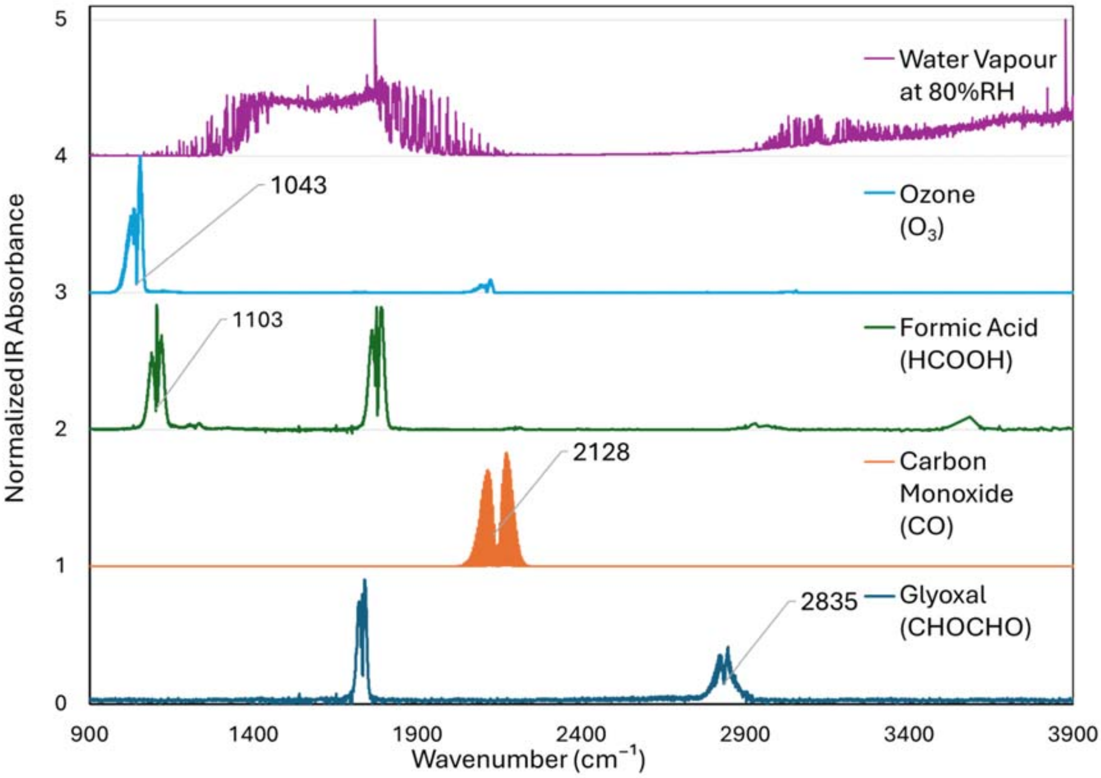

Figure S4. Result of XPS analysis of a filter sample collected during one ageing experiment of Gobi dust with glyoxal, at 80% RH (experiment D15 in Table S3). Left: XPS spectrum and derived atomic percentages. Right: zoomed view of the most prominent peaks, and their attribution. From top to bottom, and left to right: Si2p attributed to quartz in mineral dust, C1s from the C-F bond of the Teflon filter (297 eV) and from carbon in the aerosols, O1, and F1s from the C-F bond of the Teflon filter.

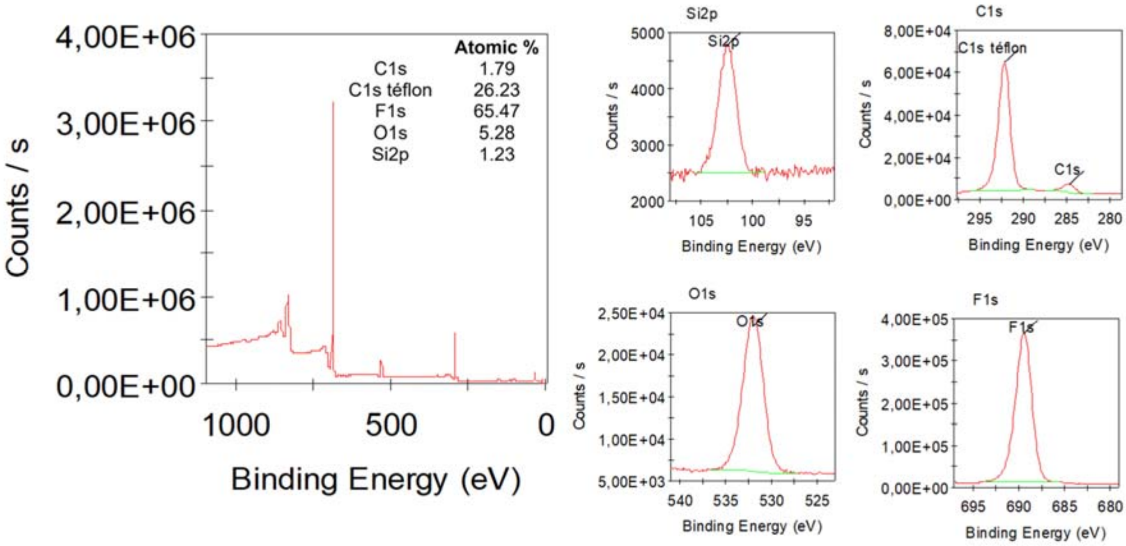

Figure S5. Inter-comparison of the measured glyoxal concentrations by the three techniques adopted in this study. The FTIR glyoxal concentration time series is represented as black dots, CAPS NO_2 concentration as a grey line and the PTR–ToF–MS intensity of the protonated glyoxal at 58.9312 m/z in number of counts per second (npcs) as a red line (Exp. 1, dry conditions).

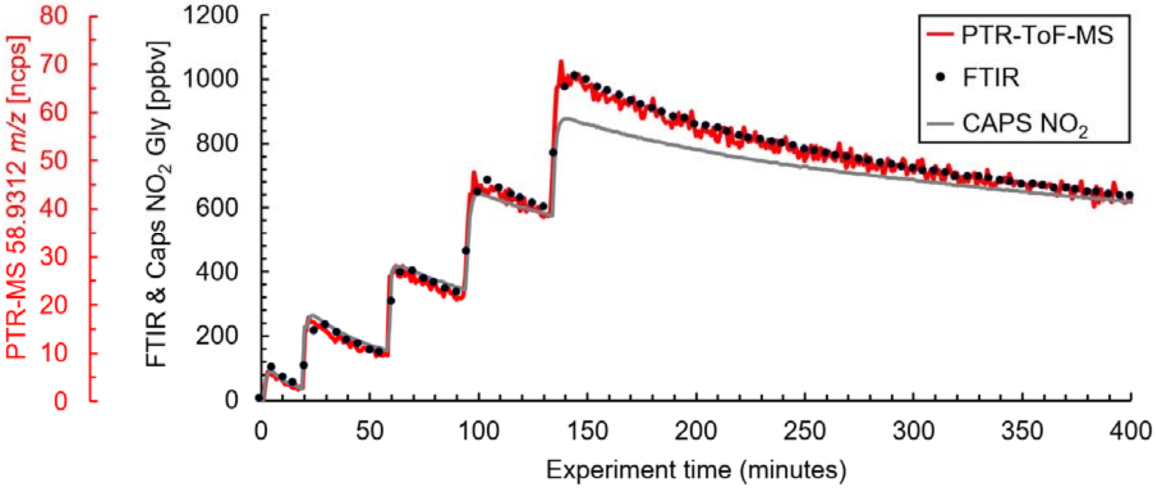

Figure S6. Correlations between the different techniques for glyoxal measurement: (a) m/z 30 and m/z 58.9 measured by PTR–MS; (b) FTIR and PTR-MS in dry (white squares) and humid (blue squares) conditions; (c) CAPS NO_2 and PTR–MS in dry condition; (d) CAPS NO_2 and FTIR in dry condition.

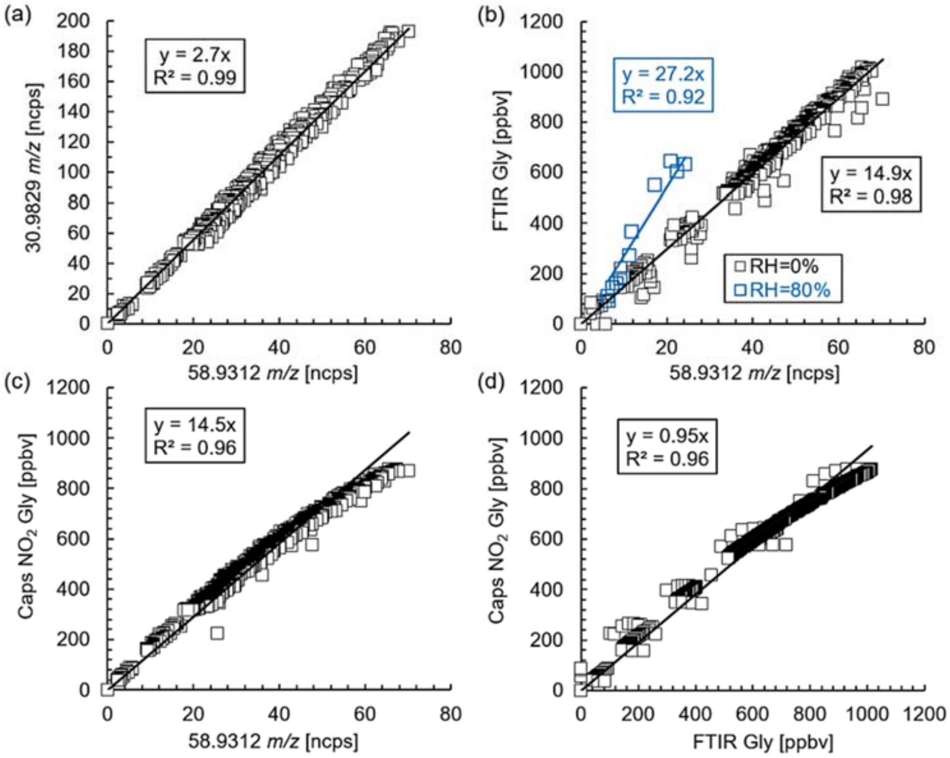

Figure S7. Comparison of glyoxal concentration profiles measured by the three techniques adopted for glyoxal monitoring in this study during a typical experiment of this study conducted under humid conditions (experiment 5). The FTIR glyoxal concentration time series is represented as white dots on a grey line, CAPS NO2 concentration as white squares on a black line, the PTR – ToF – MS intensity of the protonated glyoxal at 58.9312 m/z in number of counts per second (npcs) as orange squares on an orange line and the relative humidity level as a grey area. The moment corresponding to the injection of glyoxal in the chamber is also indicated. In the absence of water vapour, the concentrations decrease at a very similar rate, whereas under humid conditions, the concentration measured by FTIR decreases at a slower rate than PTR-MS and CAPS NO_2.

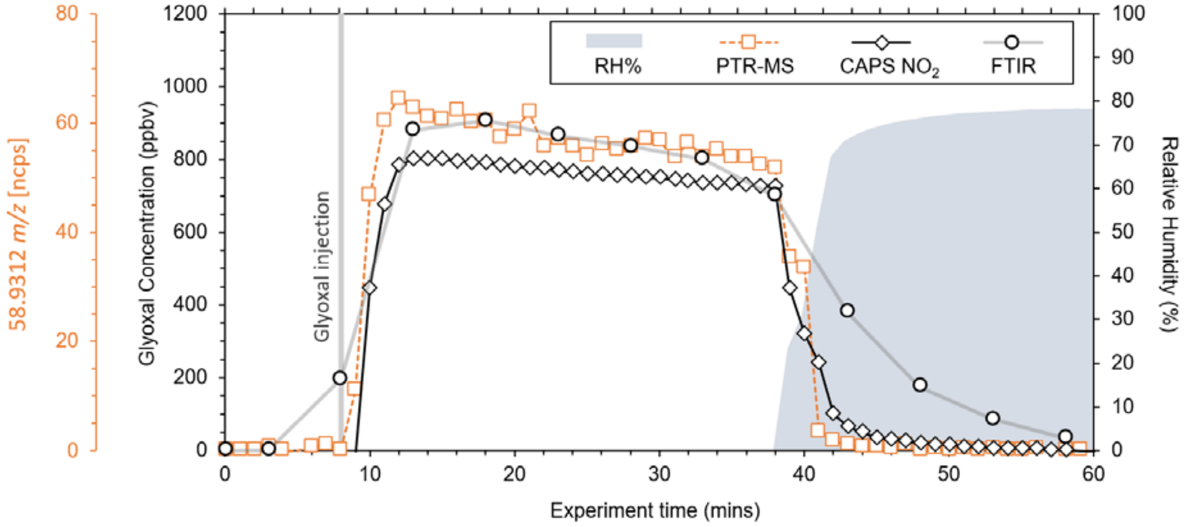

Figure S8. FTIR spectra recorded during experiment 3 in the wavenumber range 2750-2950 cm⁻¹, where the absorption due to the C-H stretching of glyoxal occurs. The grey curve represents the absorption of glyoxal before the injection of water vapour, while the blue curves (the colour intensity is proportional to the residence time in the simulation chamber) represent the evolution of the signal after the injection of water vapour into the simulation chamber with a temporal resolution of 5 minutes. The spectra are normalized on the average absorption intensity recorded in the wavenumber interval considered. The spectra here shown are subtracted from the water spectrum recorded under the same RH conditions in CESAM.

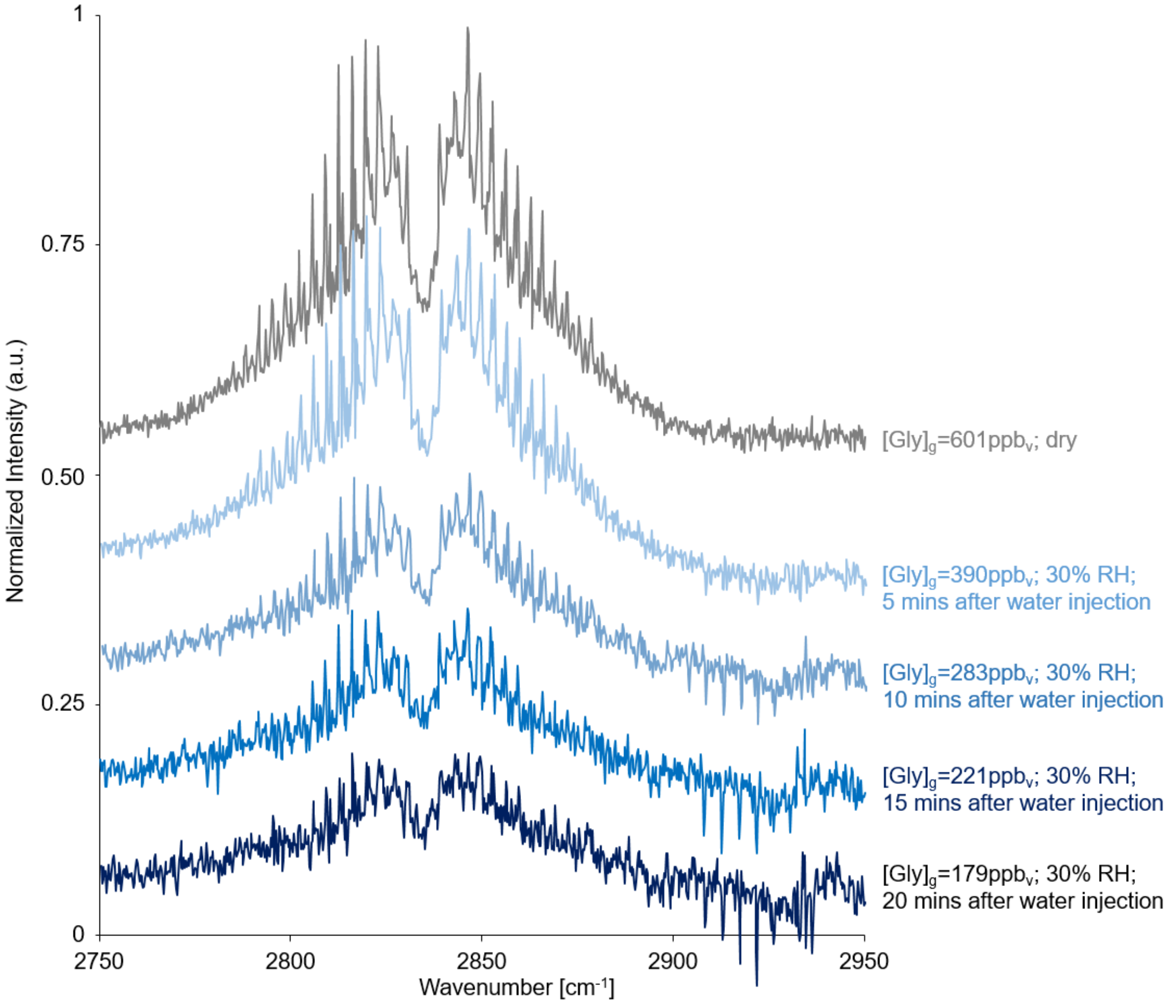

Figure S9. Time series from the results of the adopted kinetic model and the comparison with experimental data for experiment 6. In the upper graph: experimental glyoxal concentration measured by FTIR is depicted as green squares, water concentration is represented as a light blue line and the results of the model are represented by a red line and a grey line for gas phase concentration and glyoxal adsorbed on the chamber walls, respectively. In the graph below the gas phase glyoxal lost by dilution is represented by a purple line. A yellow line represents the photolysed glyoxal concentration.

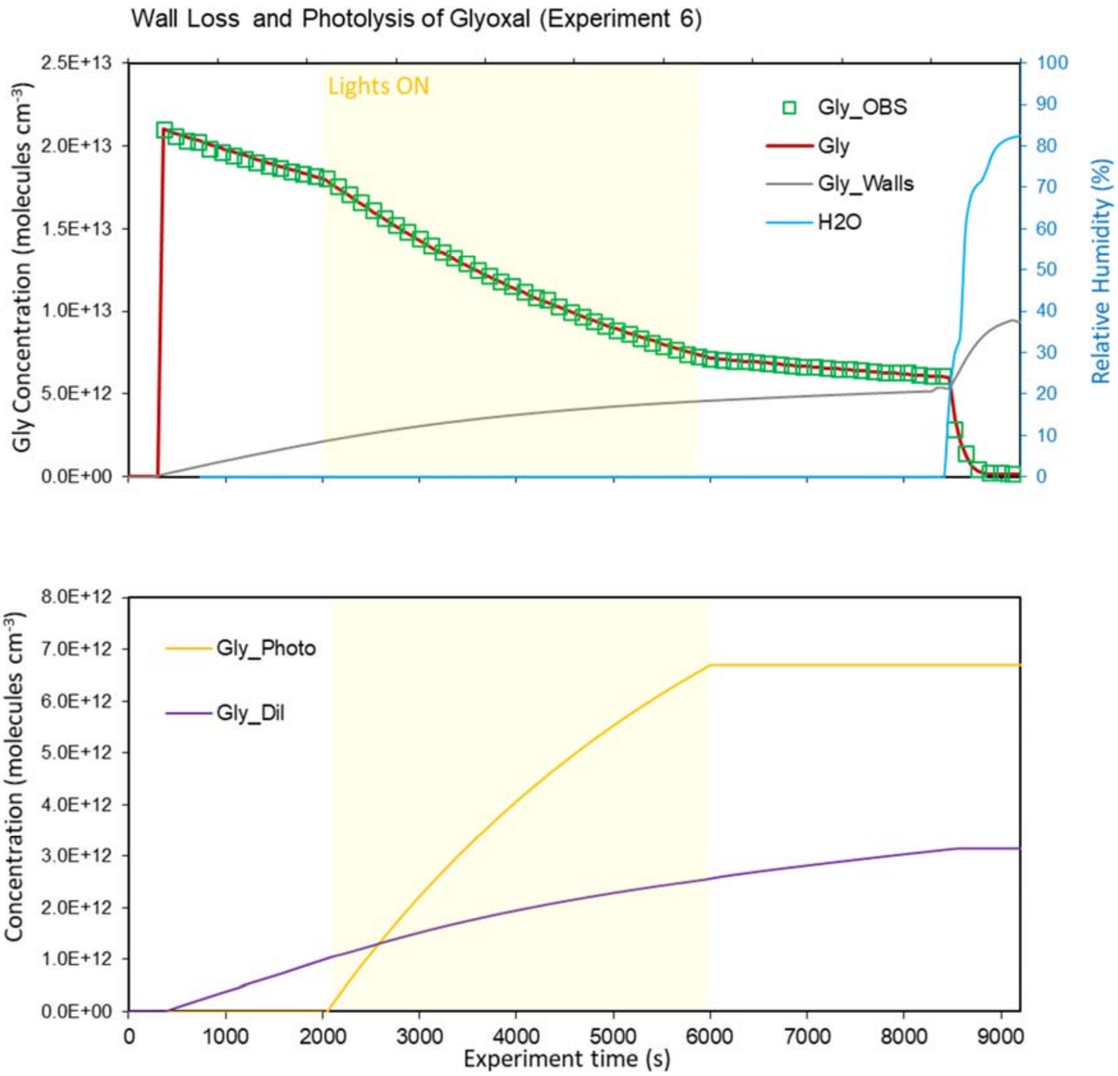

Figure S10. Size-dependent wall loss calculated of mineral dust particles (density of 2.65 g cm^{-3}) in CESAM.

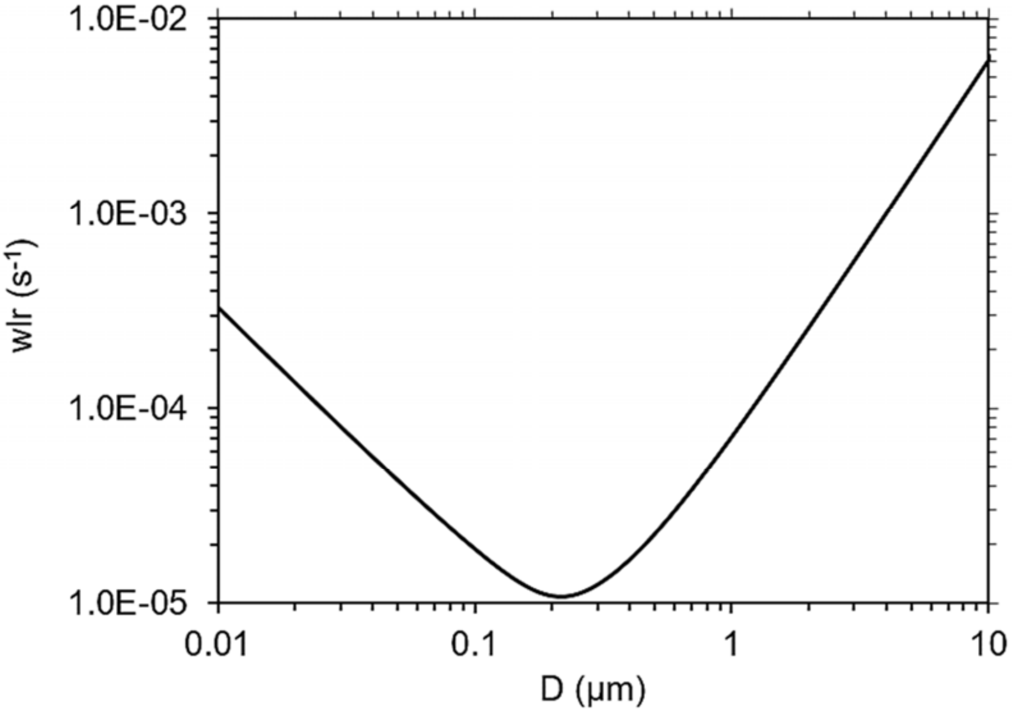

Figure S11. Size dependent Particle Loss (PL; %) calculated for mineral dust aerosols for the sampling lines connecting the simulation chamber atmosphere to ACSM (red line), OPC (green line), SMPS (black line), and CPC (black like). For mineral dust, the density used for calculations is 2.65 g cm^{-3}.

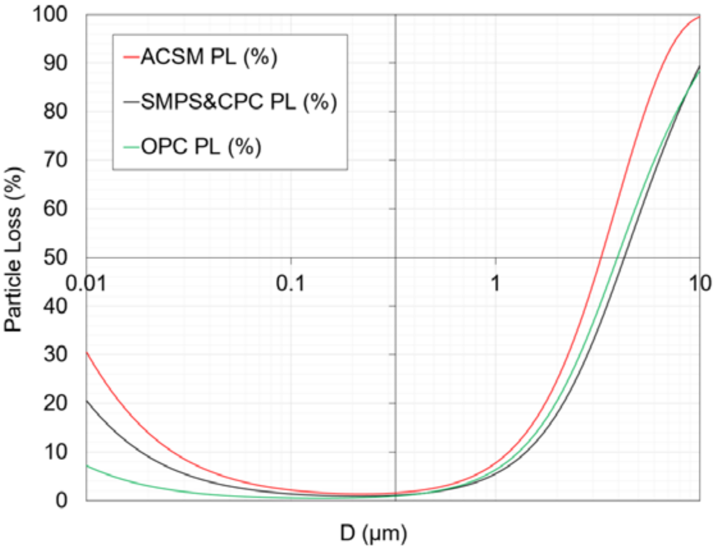

Figure S12. The time series of total organic, m/z 58, 105, and 68 fragment ions normalized by the sulphate ion signal for glyoxal uptake experiments. They mimic the graphical representation of the dilution experiments conducted in the study of Galloway et al., (2009). In our study, dilution begins almost instantaneously after glyoxal injection, as it is quantitatively lost on the walls of the chamber within a few minutes. (a) glyoxal uptake on AS at 30% RH in dark conditions, (b) glyoxal uptake on AS at 30% RH in dark conditions, (c) glyoxal uptake on AS at 30% RH under irradiated conditions after, (d) glyoxal uptake on AS at 80% RH under irradiated conditions, (e) glyoxal uptake on AS at 80% RH under irradiated conditions.

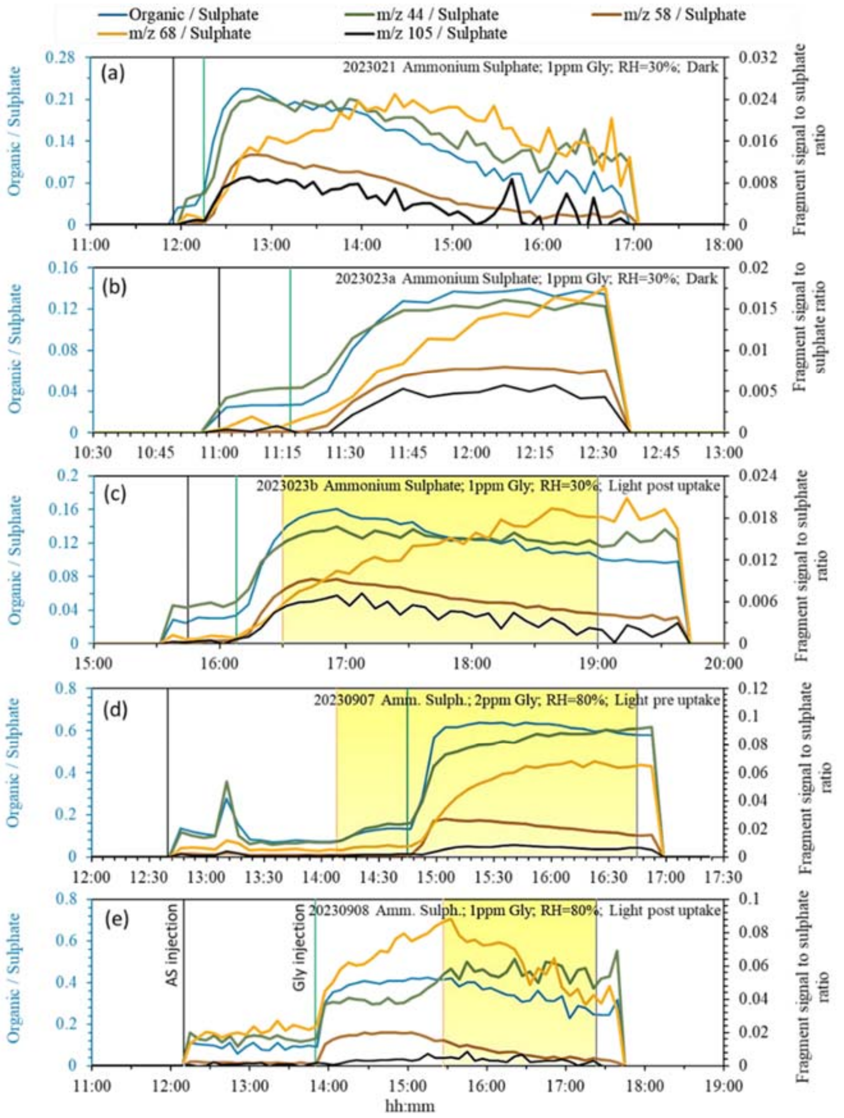

Figure S13. Time traces of glyoxal concentration, total organics, and specific fragment ions from Galloway et al. (2009). Top panel shows the time traces of glyoxal concentration, total organics, and specific fragment ions (m/z 58, 105, and 68) normalized by the sulphate ion signal in a dark experiment. Bottom panel displays the time traces of fragment ions (m/z 44, 58, 105, and 68) normalized by the sulphate ion signal in an experiment under irradiated conditions.

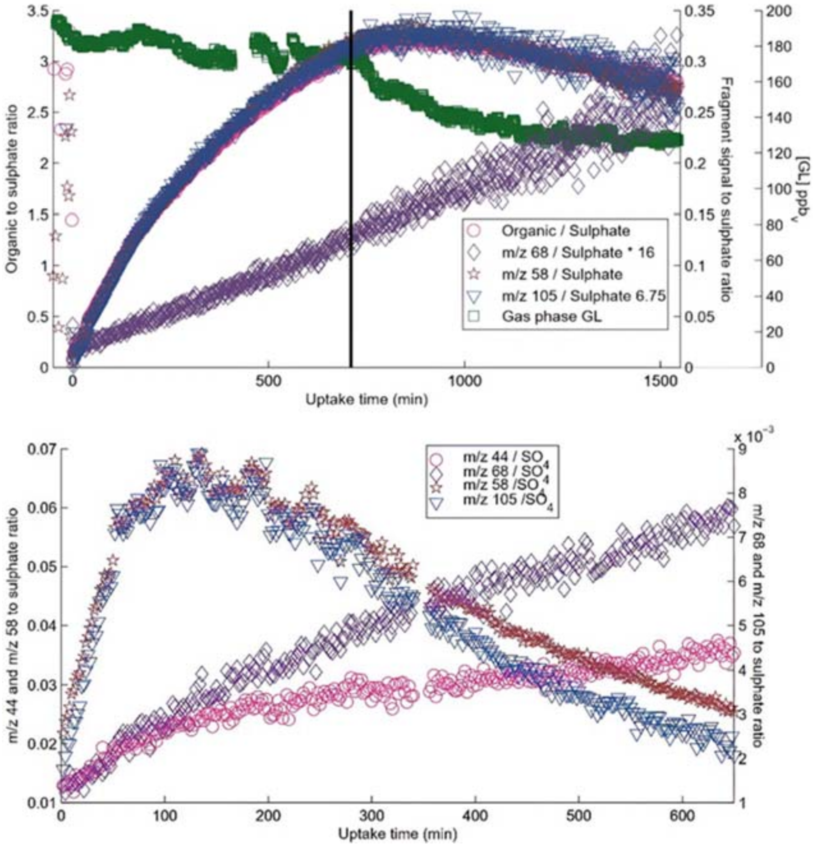

Figure S14. ACSM organic fraction mass spectra recorded at maximum glyoxal uptake on ammonium sulphate experiments: (a) glyoxal uptake on AS at 30% RH in dark conditions, (b) glyoxal uptake on AS at 30% RH in dark conditions, (c) glyoxal uptake on AS at 30% RH under irradiated conditions after, (d) glyoxal uptake on AS at 80% RH under irradiated conditions, (e) glyoxal uptake on AS at 80% RH under irradiated conditions.

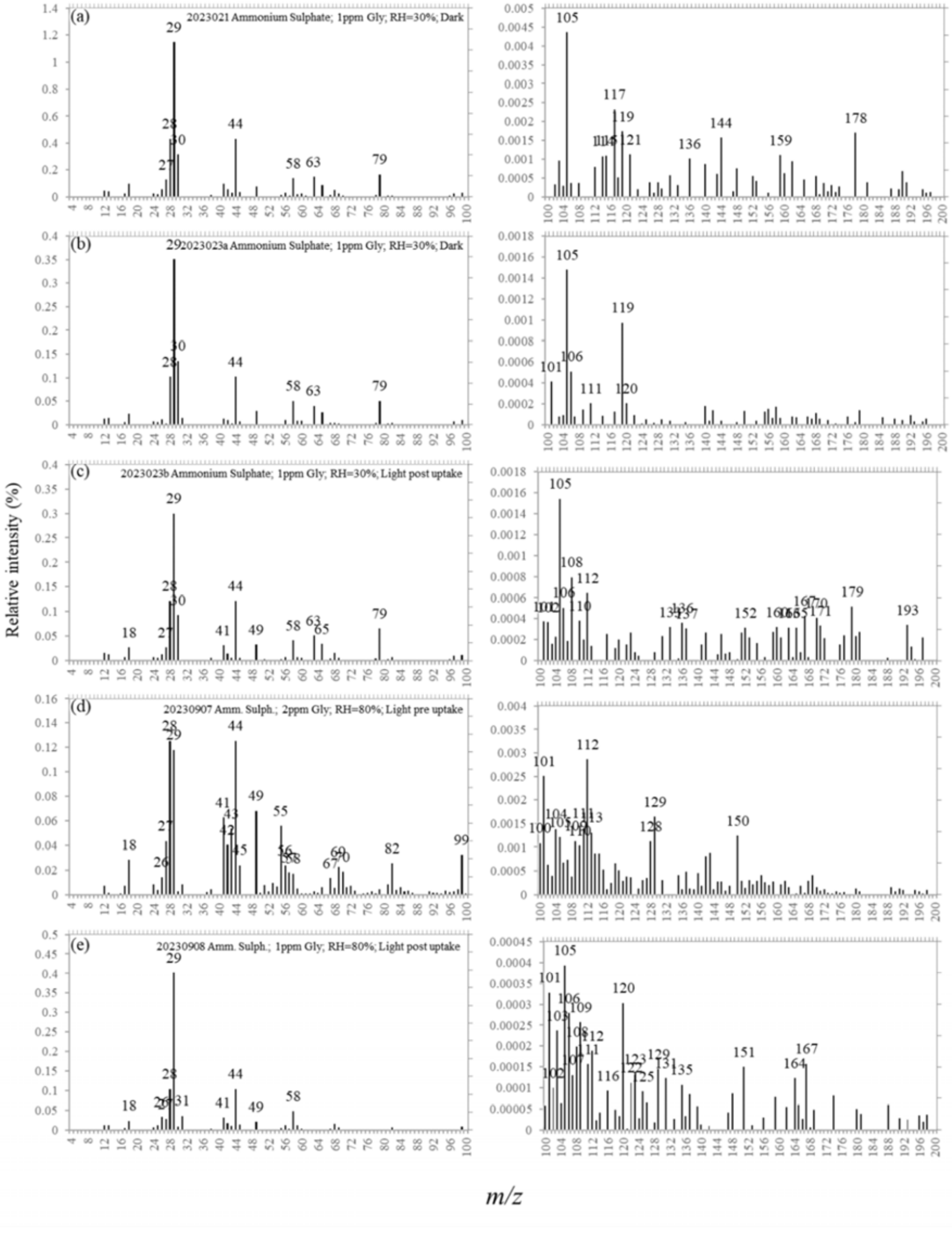

Figure S15. Timeline of the ageing experiment D_{14}, in which submicron dust was exposed to gas-phase glyoxal under humid conditions (78% RH) at 293 K and 1450 ppbv of ozone. (a) Time series of aerosol total number (grey) and volume (black) concentrations, derived from measured size distributions. (b) Mass concentrations of ammonium (yellow), sulfate (red), nitrate (blue), and organic compounds (green), as measured by the ACSM. The yellow-shaded area marks the period of irradiation, while green dashed vertical lines indicate the timing of glyoxal injection and red dashed vertical lines indicate the timing of ozone injection. All aerosol measurements have been corrected for dilution, wall losses, and losses in sampling lines.

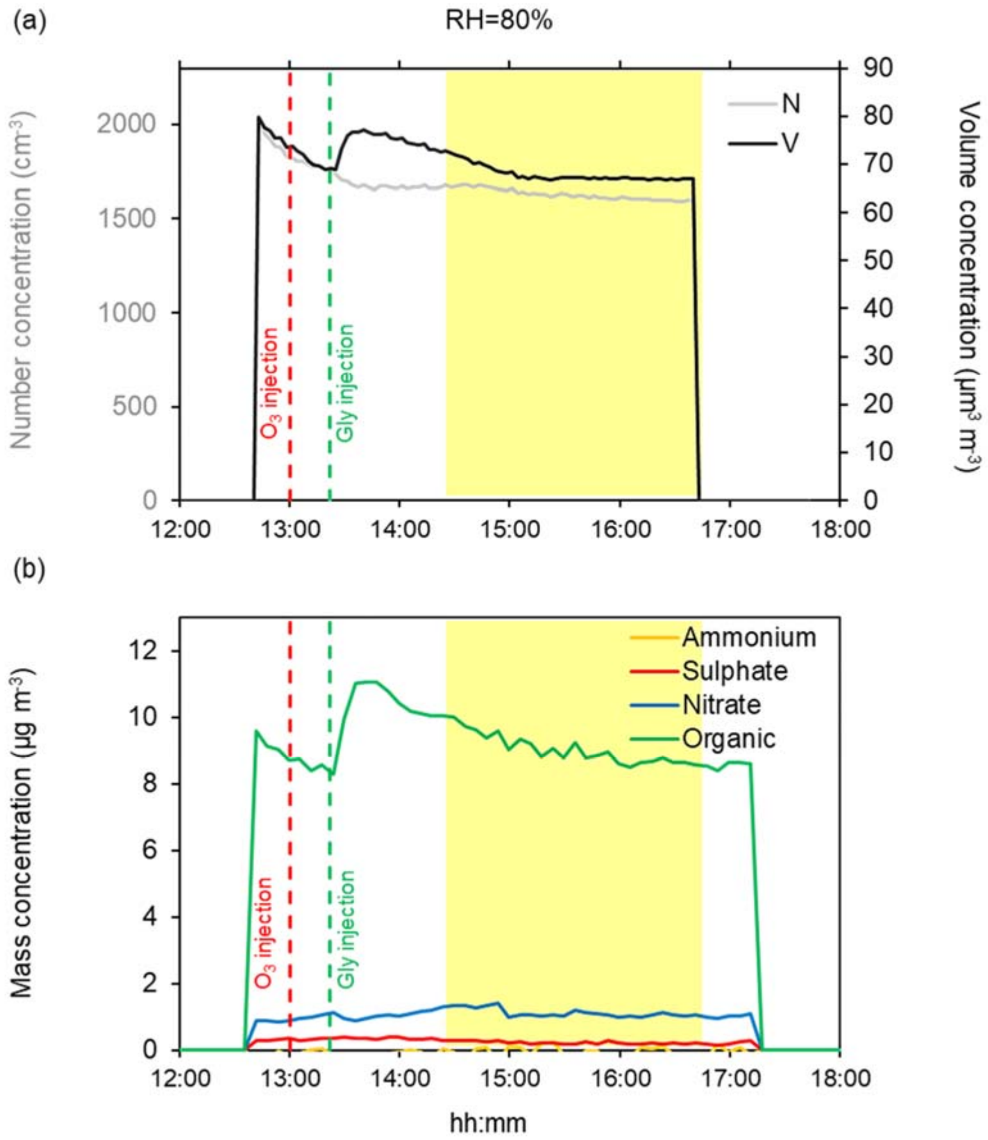

Figure S16. Comparison of the time series of the logarithm of POM concentration (normalized to the initial value POM_0), upper panel, and the total volume concentration (normalized to the initial value Vol_0), lower panel. Time is calculated since the end of the dust injection. The slope of the linear decrease during the evaporation phase (straight solid lines) is indicated.

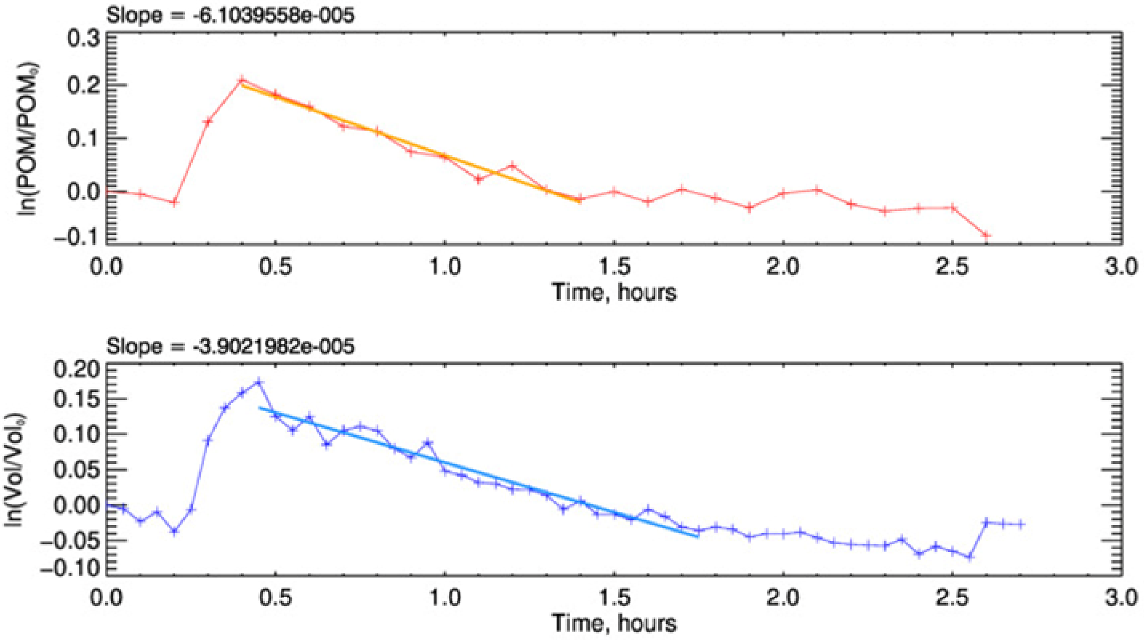

Figure S17. NO and NO_2 concentrations measured during the injection of water vapour in experiment D_{15}. The shaded area corresponds to the injection of dust into the chamber, during which the instruments were disconnected. The yellow-highlighted portions indicate the interval where irradiation takes place. Wang et al. (2011) have shown that the chamber walls may act as a reservoir of a NO and HONO, that can be rapidly desorbed during the injection of water vapour. Upon irradiation, the desorbed HONO may act as a source of OH radicals, which in turn facilitate the rapid conversion of NO to NO_2.

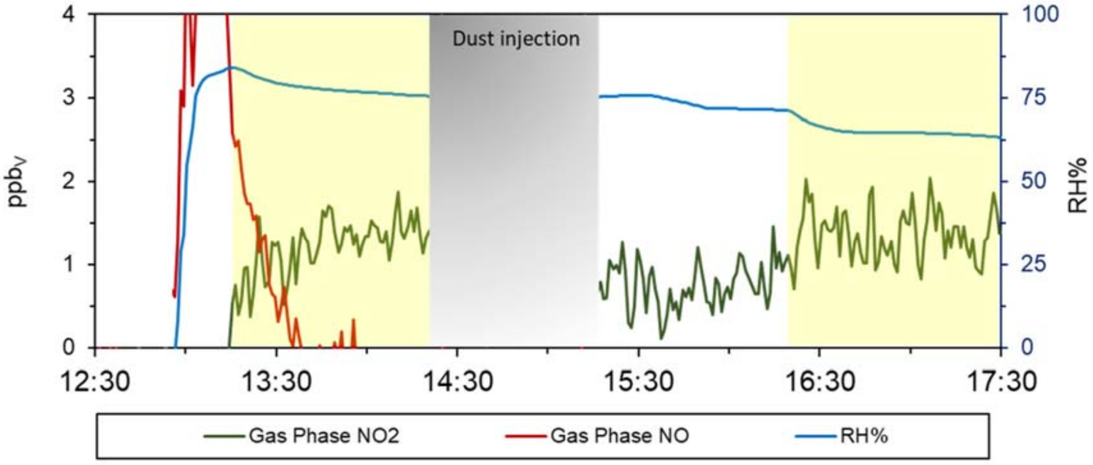

Figure S18. Organic mass spectra measured by the ACSM depicting the composition of the organic fraction of Gobi dust under different experimental conditions. The spectra are shown for (a) Gobi dust measured outside the chamber under three different relative humidity (RH) conditions, (b) Gobi dust within the chamber under dry conditions, comparing dark and irradiated states, and (c) Gobi dust within the chamber at 80% RH, also comparing dark (black bars) and irradiated states (light gray bars). The x-axis represents the mass-to-charge ratio (m/z) and the y-axis shows the normalized intensity of detected organic fragments.

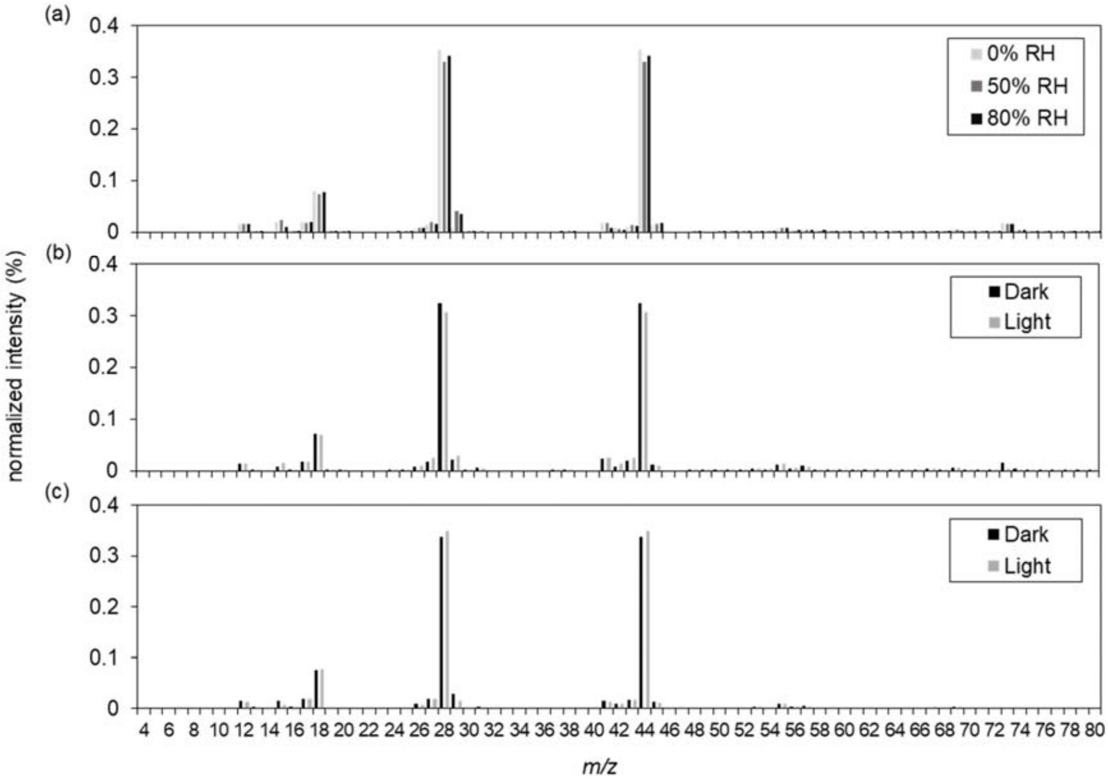

Figure S19. Orbitrap mass spectra and Van Krevelen diagrams illustrating the organic content of aerosols collected under four distinct conditions: dry conditions without and with light exposure and at 80% RH without and with light exposure. The left panels display the mass spectra; the right panels are the corresponding Van Krevelen diagrams. In these spectra, different colours correspond to specific classes of compounds: black for CHO (carbon, hydrogen, oxygen), red for CHON (carbon, hydrogen, oxygen, nitrogen), blue for CHOS (carbon, hydrogen, oxygen, sulphur), purple for CHNS (carbon, hydrogen, nitrogen, sulphur), and green for CHONS (carbon, hydrogen, oxygen, nitrogen, sulphur). These colour code is consistent across both the mass spectra and the Van Krevelen diagrams.

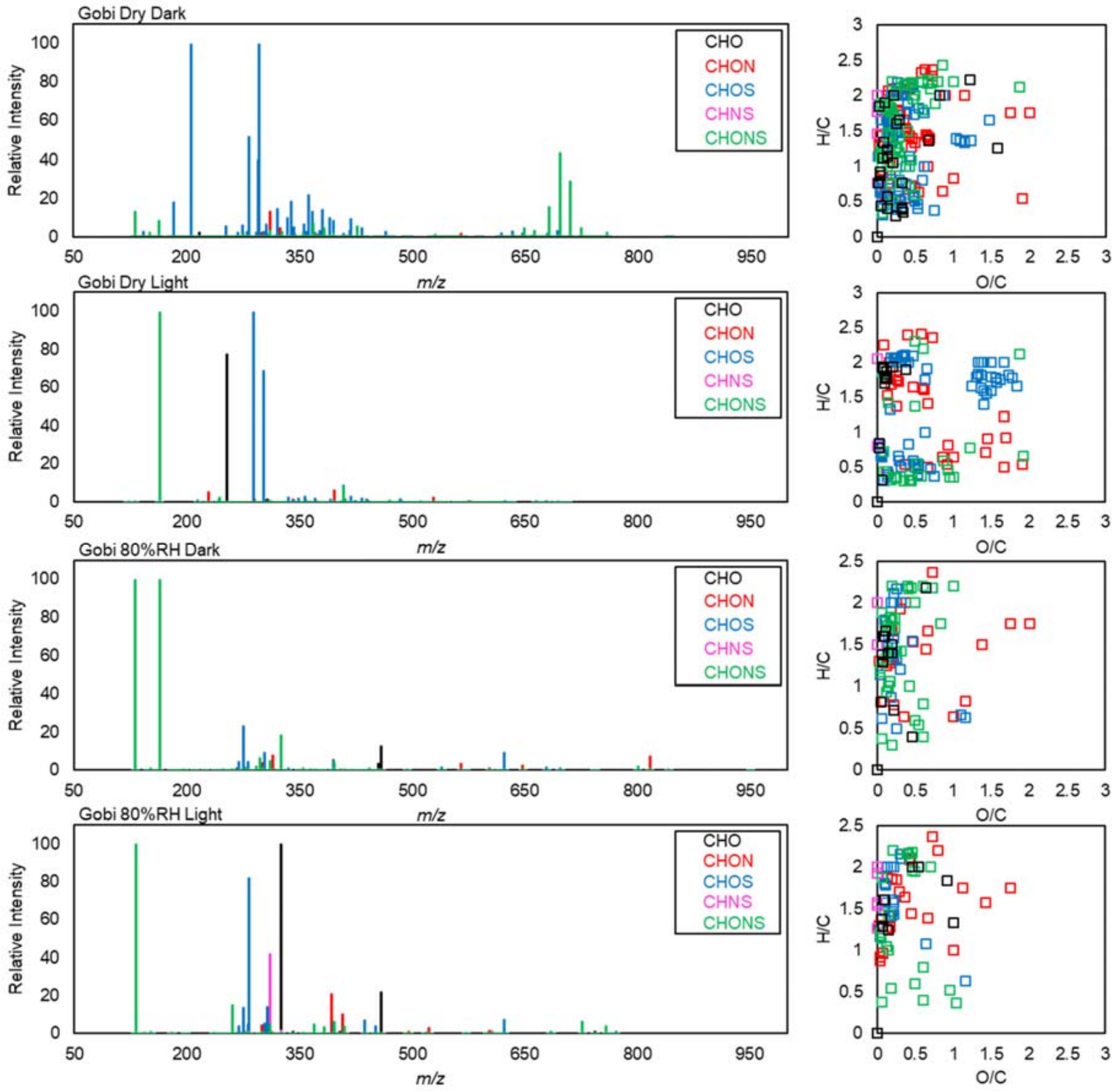

Figure S20. Chromatograms from SFE-GC-MS analysis of Gobi dust under four different conditions, from top to bottom: (1) dry, dark; (2) dry, light; (3) RH 80%, dark; (4) RH 80%, light. The retention time interval between 34 and 38 minutes was selected for analysis due to the absence of significant peaks before 34 minutes and the presence of internal standards after 38 minutes. The peaks marked with asterisks are those that remained unassigned.

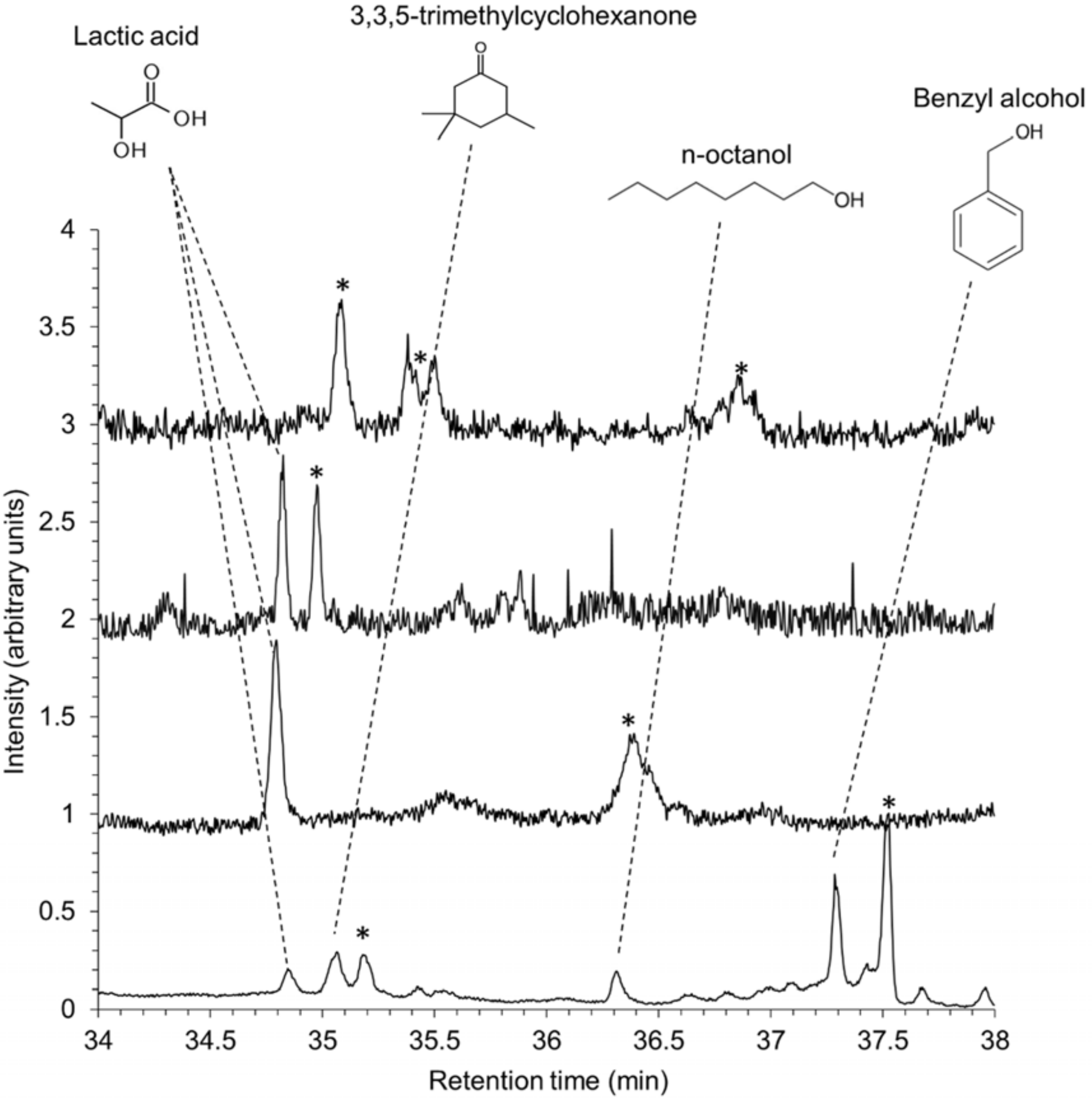

Figure S21. SFE/GC-MS chromatograms recorded from filters collected during one dust control experiment and four glyoxal uptake experiments under 80% RH and different oxidation conditions. From up to bottom: the first chromatogram is from Experiment D_2, dust control experiment with irradiation. The second is from Experiment D_{16} with dust and glyoxal under dark conditions. The third is from Experiment D_{15} with dust and glyoxal with irradiation. The fourth and fifth chromatograms are from Experiment D_{13} with dust and glyoxal in the presence of ozone under dark and irradiated conditions, respectively. The two peaks of higher intensity appearing after 41 minutes are from the internal standards added to the solution: tridecane around 41 minutes and ortho-toluic acid at about 41.8 minutes. The intensity is normalized to peak of the internal standard ortho-toluic acid. The chromatograms start at 32 minutes as 15 minutes are required for the removal of CO_2 from the extraction fluid, and approximately another 15 minutes represent the delay required for the solvent to pass through the column and reach the electron ionization (EI) MS detection. For the second and third spectra, is noticeable that under irradiated conditions the number of peaks increases significantly compared to dark conditions, likely due to enhanced chemical reactions driven by light. This effect appears to be less pronounced in the presence of ozone.

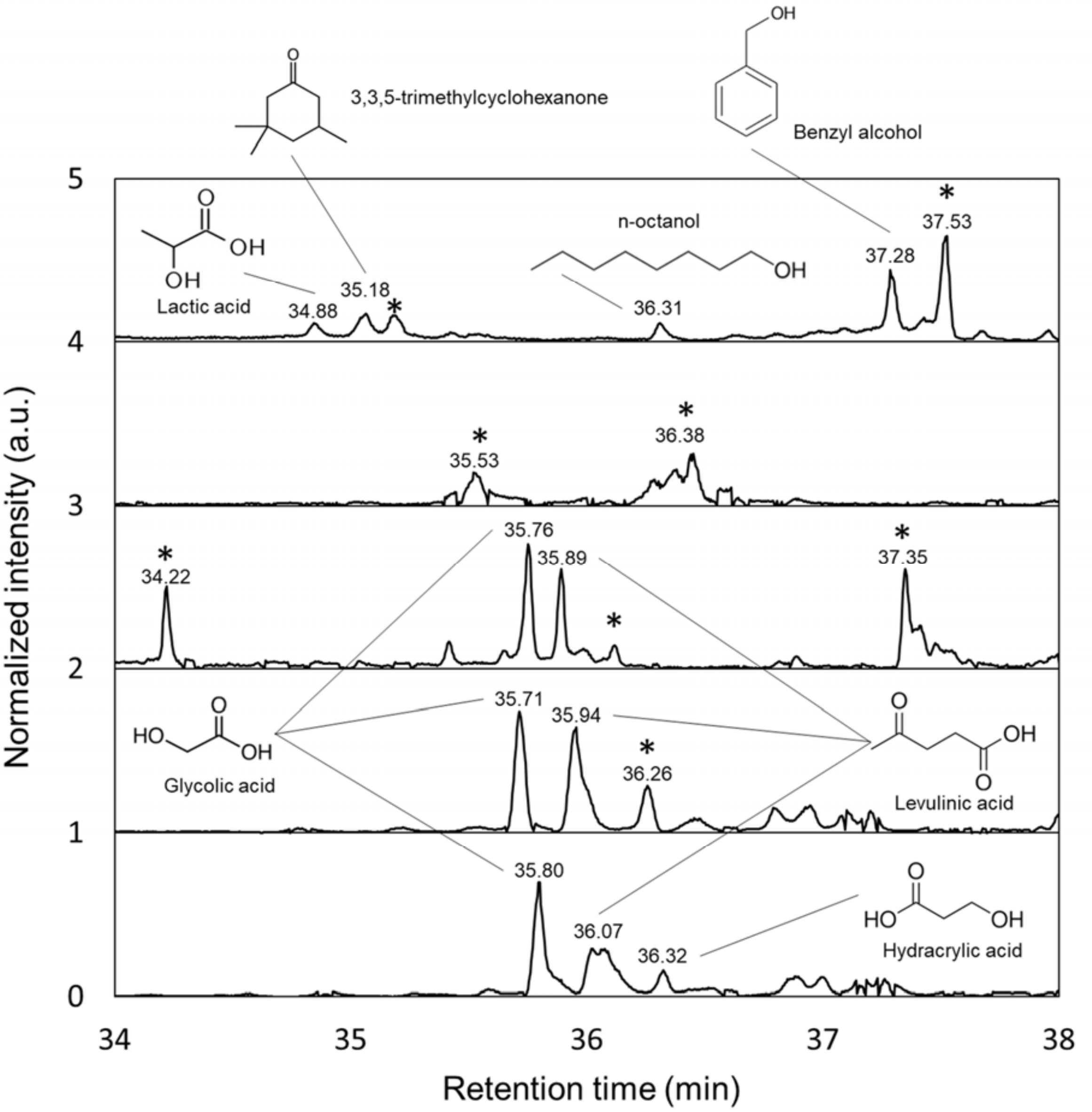
3,3,5-trimethylcyclohexanone
O
OH
Benzyl alcohol
Lactic acid
O
OH
OH
34.88
35.18
*
n-octanol
OH
36.31
37.28
*
37.53
*
35.53
*
36.38
*
34.22
35.76
35.89
*
*
37.35
HO
O
OH
Glycolic acid
35.71
35.94
*
36.26
O
OH
O
Levulinic acid
35.80
36.07
36.32
O
HO
OH
Hydracrylic acid
Normalized intensity (a.u.)
5
4
3
2
1
0
34
35
36
37
38
Retention time (min)

Figure S22. ESI Orbitrap MS from the filter D_{10}: uptake of glyoxal on mineral dust at 80% RH and under irradiation. In the mass spectra, the peaks referring to formulas for which is possible to suggest a structure from glyoxal reactivity are labelled.

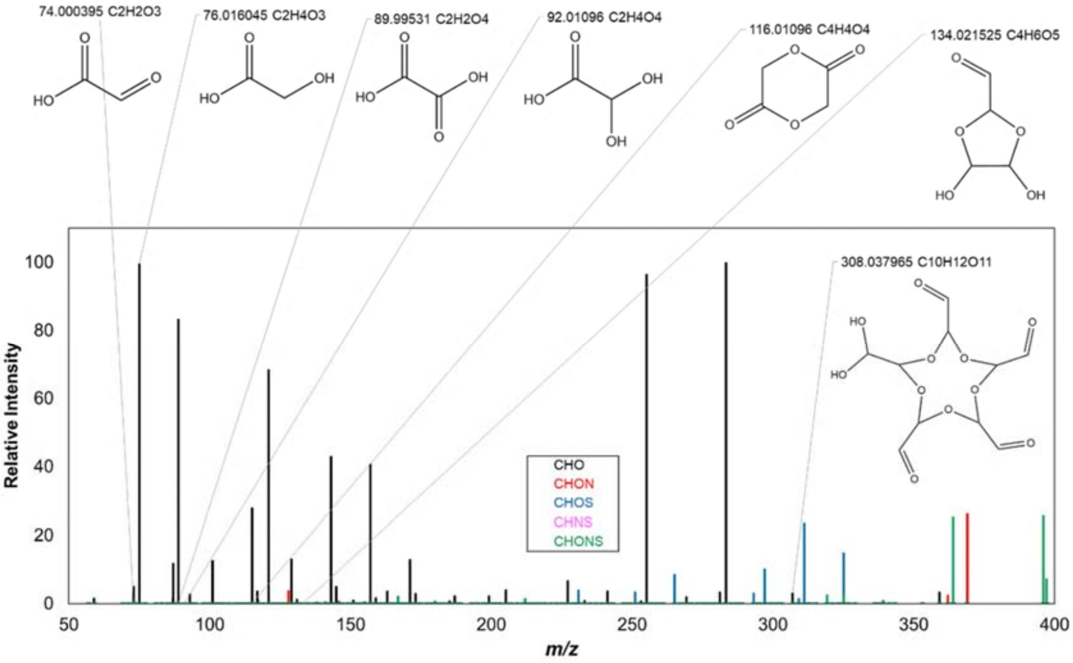

Table S1. Characteristics of the instrumental and analytical setup for the analysis of the gas and aerosol phases presented in this study.

Instrument	Function	Characteristics
FTIR Spectrometer (Bruker Tensor 37)	Gas-phase composition (glyoxal, formic acid, CO, O_3)	Glyoxal quantified from C-H bond stretching (2720–2930 cm^{-1}) Time resolution: 5 min Spectral range: 700 – 4000 cm^{-1} (resolution: 0.5 cm^{-1}; optical path length: 120 m)
CAPS NO_2 Analyzer (Teledyne API T500U)	Gas-phase glyoxal	Absorption at 450 nm Time resolution: 30 sec Concentration range 10 – 1000 ppbv
PTR-ToF-MS (KORE Technology)	VOCs with H_3O^+ ionization	Operated at a reactor pressure of 1.35 mbar and temperature of 60°C, E/N ratio of 131 Td; Time resolution: 1 min Concentration depends on species
NO_x Analyzer (Horiba APNA-370)	NO_x concentration	Time resolution: 1 min Sampling flow: 0.8 L min^{-1}; Concentration range 1 – 1000 ppb
CO/CO_2 Analyzer (APEE ProCeas®)	CO/CO_2 concentrations	Time resolution: 1 min Sampling flow: 0.2 L min^{-1}; Concentration range 100 ppb – 1 ppm (CO), 50 ppb – 1 ppm (CO_2)
Condensation Particle Counter (TSI 3075)	Particle total number concentration	Condensation growth and optical detection Time resolution: 1 sec Sampling flow: 1.5 L min^{-1}; Size range 2.5 nm-3 μm
Scanning Mobility Particle Sizer (TSI 3080)	Particle number size distribution	Particle electrical mobility Time resolution: 3 min Aerosol flow/sheath flow: 0.3/3.0 L min^{-1}; Size range 19.5 – 881.7 nm (107 channels)
Optical Particle Counter (sky-GRIMM 1.109)	Particle number size distribution	Particle optical detection Time resolution: 12 sec Aerosol flow: 1.2 L min^{-1}; Laser wavelength: 655 nm; Size range 0.265 μm – 31 μm (31 channels)
ToF-ACSM (Aerodyne)	Aerosol non-refractory chemical composition	Ionization via electron impact at ~600°C Time resolution: 6 min Size range 40 nm – 1 μm
Filter Sampling	Filter samples for offline analysis	Time resolution: 30 min-3 hours Filters: PTFE and quartz; Sampling flow: 10 L min^{-1}
SFE/GC-MS (Supercritical Fluid Extraction)	Molecular composition of aerosol organic fraction	Extraction using supercritical CO2; m/z 50–500, m/z 150–1000
ESI High-Resolution MS (Orbitrap)	Molecular composition of aerosol organic fraction	Ions are generated with electrospray ionization (ESI) from aerosol organic compounds, separated by their mass-to-charge ratio using electrostatic trapping in an Orbitrap analyzer, allowing precise determination of molecular composition at high mass resolution. High mass resolution (100,000 at m/z 400); m/z 50–500, m/z 150–1000
XPS (VG ES-CALAB 250)	Elemental O/C ratio of particle surface.	Utilizes monochromatic Al K_α radiation (1486.6 eV) Surface depth < 10 nm

Table S3. List of filter samples collected for SFE-GC-MS and Orbitrap high-resolution mass spectrometry analyses, along with the corresponding experimental conditions. The experiments include dust only (D) and dust combined with glyoxal (D + GL). For selected experiments, filters were collected both in the dark or during irradiation (light). The RH values refer to the average relative humidity measured during the respective filter sampling periods. The presence of ozone (O_3) is indicated in the "Ox" column.

Conditions	ID	Date	RH (%)	Light	Ox	Orbitrap	SFE
D	D_1	31/01/2022	<5	dark	---	**X**	**X**
				light	---	**X**	**X**
D	D_2	03/02/2022	75	dark	---	**X**	**X**
				light	---	**X**	**X**
D + GL	D_3	04/02/2022	<5	dark	---	**X**	**X**
				light	---	**X**	**X**
	D_4	08/02/2023	32	dark	---		**X**
	D_5	09/02/2023	31	light	---	**X**	**X**
	D_6	10/02/2023	35	dark	---	---	**X**
	D_7	13/02/2023	34	light	---	---	**X**
	D_8	30/04/2021	76	light	---	---	---
	D_9	03/05/2021	79	light	---	---	---
	D_{10}	04/05/2021	81	light	---	**X**	---
	D_{11}	05/05/2021	78	dark	---	**X**	---
	D_{12}	06/05/2021	82	dark	---	**X**	---
	D_{13}	08/02/2022	81	dark	O_3	**X**	**X**
				light		**X**	**X**
	D_{14}	09/02/2022	78	dark	O_3	---	---
				light		**X**	**X**
	D_{15}	10/02/2022	75	dark	---	---	---
				light	---	**X**	**X**
	D_{16}	14/02/2023	83	dark	---	**X**	**X**
	D_{17}	15/02/2023	75	light	---	---	**X**

References of the Supplementary Material

Atkinson, R., Baulch, D. L., Cox, R. A., Crowley, J. N., Hampson, R. F., Hynes, R. G., Jenkin, M. E., Rossi, M. J., and Troe, J.: Evaluated kinetic and photochemical data for atmospheric chemistry: Volume I - gas phase reactions of Ox, HOx, NOx and SOx species, Atmos. Chem. Phys., 4, 1461–1738, https://doi.org/10.5194/acp-4-1461-2004, 2004.

Atkinson, R., Baulch, D. L., Cox, R. A., Crowley, J. N., Hampson, R. F., Hynes, R. G., Jenkin, M. E., Rossi, M. J., Troe, J., and IUPAC Subcommittee: Evaluated kinetic and photochemical data for atmospheric chemistry: Volume II – gas phase reactions of organic species, Atmos. Chem. Phys., 6, 3625–4055, https://doi.org/10.5194/acp-6-3625-2006, 2006.

Carr, F. J., Chill, D., and Maida, N.: The Lactic Acid Bacteria: A Literature Survey, Critical Rev. Microbiology, 28, 281–370, https://doi.org/10.1080/1040-840291046759, 2002.

Denjean, C., Formenti, P., Picquet-Varrault, B., Pangui, E., Zapf, P., Katrib, Y., Giorio, C., Tapparo, A., Monod, A., Temime-Roussel, B., Decorse, P., Mangeney, C., and Doussin, J. F.: Relating hygroscopicity and optical properties to chemical composition and structure of secondary organic aerosol particles generated from the ozonolysis of α-pinene, Atmos. Chem. Phys., 15, 3339–3358, https://doi.org/10.5194/acp-15-3339-2015, 2015.

Doussin, J.-F., Fuchs, H., Kiendler-Scharr, A., Seakins, P., & Wenger, J. (Eds.). (2023). A Practical Guide to Atmospheric Simulation Chambers. Springer International Publishing. https://doi.org/10.1007/978-3-031-22277-1

Galloway, M. M., Chhabra, P. S., Chan, A. W. H., Surratt, J. D., Flagan, R. C., Seinfeld, J. H., and Keutsch, F. N.: Glyoxal uptake on ammonium sulphate seed aerosol: reaction products and reversibility of uptake under dark and irradiated conditions, Atmos. Chem. Phys., 9, 3331-3345, 10.5194/acp-9-3331-2009, 2009.

Gardner, E. P., Sperry, P. D., and Calvert, J. G.: Primary quantum yields of NO2 photodissociation, J. Geophys. Res., 92, 6642–6652, https://doi.org/10.1029/JD092iD06p06642, 1987.

Gonçalves, C., Alves, C., Nunes, T., Rocha, S., Cardoso, J., Cerqueira, M., Pio, C., Almeida, S. M., Hillamo, R., and Teinilä, K.: Organic characterisation of PM10 in Cape Verde under Saharan dust influxes, Atmos. Environ., 89, 425–432, https://doi.org/10.1016/j.atmosenv.2014.02.025, 2014.

Grosjean, D.? Wall loss of gaseous pollutants in outdoor Teflon chambers. Environmental Science & Technology, 19(11), 1059–1065. https://doi.org/10.1021/es00141a006, 1985.

Jung, C. and Schindler, D.: The role of air density in wind energy assessment – A case study from Germany, Energy, 171, 385–392, https://doi.org/10.1016/j.energy.2019.01.041, 2019.

Kawamura, K., Steinberg, S., and Kaplan, I. R.: Homologous series of C1–C10 monocarboxylic acids and C1–C6 carbonyls in Los Angeles air and motor vehicle exhausts, Atmos. Environ., 34, 4175–4191, https://doi.org/10.1016/S1352-2310(00)00212-0, 2000.

Kim, H. J., Kim, B. C., Park, H., Cho, G., Lee, T., Kim, H. T., Bhatia, S. K., and Yang, Y.-H.: Microbial production of levulinic acid from glucose by engineered Pseudomonas putida KT2440, J. Biotechnology, S016816562400258X, https://doi.org/10.1016/j.jbiotec.2024.09.015, 2024.

Kostenidou, E., Pathak, R. K., and Pandis, S. N.: An Algorithm for the Calculation of Secondary Organic Aerosol Density Combining AMS and SMPS Data, Aeros. Sci. Tech., 41, 1002–1010, https://doi.org/10.1080/02786820701666270, 2007.

Kourtchev, I., Doussin, J.-F., Giorio, C., Mahon, B., Wilson, E. M., Maurin, N., Pangui, E., Venables, D. S., Wenger, J. C., and Kalberer, M.: Molecular composition of fresh and aged secondary organic aerosol from a mixture of biogenic volatile compounds: a high-resolution mass spectrometry study, Atmos. Chem. Phys., 15, 5683–5695, https://doi.org/10.5194/acp-15-5683-2015, 2015.

Lai, A. C., Nazaroff, W. W. Modeling indoor particle deposition from turbulent flow onto smooth surfaces. J. Aerosol Sci., 31(4), 463-476, 2000.

Lamkaddam, H., Gratien, A., Pangui, E., Cazaunau, M., Picquet-Varrault, B., and Doussin, J.-F.: High-NOx Photooxidation of n-Dodecane: Temperature Dependence of SOA Formation, 51, 192–201, https://doi.org/10.1021/acs.est.6b03821, 2017

Lasdon, Leon S.; Fox, Richard L.; Ratner, Margery W. Nonlinear optimization using the generalized reduced gradient method. Revue française d'automatique, informatique, recherche opérationnelle. Recherche opérationnelle, 8, V3, 73-103. https://www.numdam.org/item/RO_1974__8_3_73_0/, 1974.

Liggio, J.: Reactive uptake of glyoxal by particulate matter, J. Geophys. Res., 110, D10304, https://doi.org/10.1029/2004JD005113, 2005.

Loza, C. L., Chan, A. W. H., Galloway, M. M., Keutsch, F. N., Flagan, R. C., and Seinfeld, J. H.: Characterization of Vapor Wall Loss in Laboratory Chambers, Environ. Sci. Technol., 44, 5074–5078, https://doi.org/10.1021/es100727v, 2010.

Min, K.-E., Washenfelder, R. A., Dubé, W. P., Langford, A. O., Edwards, P. M., Zarzana, K. J., Stutz, J., Lu, K., Rohrer, F., Zhang, Y., & Brown, S. S., A broadband cavity enhanced absorption spectrometer for aircraft measurements of glyoxal, methylglyoxal, nitrous acid, nitrogen dioxide, and water vapor. Atmos. Meas. Tech., 9, 423–440. https://doi.org/10.5194/amt-9-423-2016, 2016.

Mochizuki, T., Kawamura, K., Aoki, K., and Sugimoto, N.: Long-range atmospheric transport of volatile monocarboxylic acids with Asian dust over a high mountain snow site, central Japan, Atmos. Chem. Phys., 16, 14621–14633, https://doi.org/10.5194/acp-16-14621-2016, 2016.

Mochizuki, T., Kawamura, K., Miyazaki, Y., Kunwar, B., and Boreddy, S. K. R.: Distributions and sources of low-molecular-weight monocarboxylic acids in gas and particles from a deciduous broadleaf forest in northern Japan, Atmos. Chem. Phys., 19, 2421–2432, https://doi.org/10.5194/acp-19-2421-2019, 2019.

Stönner, C., Derstroff, B., Klüpfel, T., Crowley, J. N., & Williams, J.: Glyoxal measurement with a proton transfer reaction time of flight mass spectrometer (PTR-TOF-MS): Characterization and calibration. J. Mass Spec., 52, 30–35, https://doi.org/10.1002/jms.3893, 2017.

Tadić, J., Moortgat, G. K., and Wirtz, K.: Photolysis of glyoxal in air, J. Photochem. Photobiol. A: Chemistry, 177, 116–124, https://doi.org/10.1016/j.jphotochem.2005.10.010, 2006.

von der Weiden, S.-L., Drewnick, F., and Borrmann, S.: Particle Loss Calculator – a new software tool for the assessment of the performance of aerosol inlet systems, Atmos. Meas. Tech., 2, 479–494, https://doi.org/10.5194/amt-2-479-2009, 2009.

Wang, J., Doussin, J. F., Perrier, S., Perraudin, E., Katrib, Y., Pangui, E., and Picquet-Varrault, B.: Design of a new multi-phase experimental simulation chamber for atmospheric photosmog, aerosol and cloud chemistry research, Atmos. Meas. Tech., 4, 2465–2494, https://doi.org/10.5194/amt-4-2465-2011, 2011.

Zielinski, A. T., Kourtchev, I., Bortolini, C., Fuller, S. J., Giorio, C., Popoola, O. A. M., Bogialli, S., Tapparo, A., Jones, R. L., and Kalberer, M.: A new processing scheme for ultra-high resolution direct infusion mass spectrometry data, Atmos. Environ., 178, 129–139, https://doi.org/10.1016/j.atmosenv.2018.01.034, 2018.